Finite Element Splitting Methods Applied to Incompressible Navier-Stokes flow solvers and introduction to Mixed Mass Method

By

Sudantha Balage

A Thesis

In The Department

Of

Mechanical and Industrial Engineering

Presented in Partial Fulfilment of the Requirements
For the Degree of Master of Applied Science (Mechanical Engineering) at
Concordia University
Montreal, Quebec, Canada

April 2006

Your file Votre référence
ISBN: 0-494-14296-0
Our file Notre référence
ISBN: 0-494-14296-0

ABSTRACT

Sudantha Balage

Splitting Methods are considered to be a strong candidate for obtaining accurate, robust and computationally efficient incompressible Navier-Stokes (NS) solvers based on Finite Element Method. The type of spatial errors such as the *numerical boundary layer* observed on pressure solution near walls is known to affect the stability of NS solvers. The inclusion of stabilization terms such as upwinding or artificial viscosity terms would adversely affect the accuracy of the solver. NS solvers based on LBB compliant elements, such as Taylor Hood (TH) elements do not require stabilization terms to simulate higher Reynolds number flow provided their robustness is not affected by above mentioned type of error. This motivates the study of Splitting Methods based on Taylor Hood elements with the emphasis on how well they handle numerical boundary layer type errors to obtain highly accurate NS flow solvers. The effect of the enrichment of the TH elements with pressure bubble nodes is also investigated. The present work brings several well-known Splitting Methods under a common theoretical framework and classifies them appropriate to the study. A new technique named Mixed Mass Method (M3) is introduced. Recently published works of equivalences of the previous techniques are discussed. Based on the classification, three Fractional Splitting Methods (FSM) and one Consistent Splitting Method representing a larger number of techniques are implemented in computer program. Comparative accuracies of momentum, pressure and continuity between the methods are discussed. The spatial error distribution of the pressure and its conjugate problem of the continuity are also discussed.

The FSM based on approximate pressure method was observed to have the numerical boundary layer in pressure and a similar error manifested in continuity. Guermond's Consistent Pressure Method, as reported for Spectral Elements, is found to have no pressure boundary layer for TH elements. Both methods however, have large errors in both continuity and pressure for vortical flows. FSM that uses the weak form of the split consistently (classical methods) had near machine accuracy for continuity of the flows studied. The numerical boundary layer is observed in classical pressure methods using TH elements as well. However, when TH+Pbubble element are used, the numerical boundary layer is eliminated though error in L_2 norm remained high for the test flow used. Bubble nodes were also found to increase the accuracy of velocity but not always the pressure. Present work concludes that approximate pressure methods are weaker in comparison to classical pressure methods in high Reynolds number flows.

ACKNOWLEDGEMENT

I would like to express my heartfelt gratitude to my sister Iresha Fletcher and my brother Balage Nishanatha Amarasena. Without their regular encouragement and financial support this work simply would not have been possible. I have learned much from both in dealing with adversity where their *can do* attitude had been a great inspiration to me.

I would like to thank my colleague Tao Xu for illuminating discussions on various aspects of my research during my visits to University of Toronto. I have deeply valued and benefited from Tao's gracious critique of my ideas and work.

I would also like to thank my old friends Kurt Zubatiuk and Heather Wood who welcomed my cat Michchi and me to their home during my visits to Toronto to do research work with Tao. Kurt and Heather had been the strongest supporters of my various projects and the past two years has been no exception. I would also like to acknowledge both of them for suggesting corrections and advising on typesetting for this thesis.

Thesis writing is often said to be a lonely process. In my case, I was blessed with a constant companion who insisted on staying up all night with me whenever I did so. She found playfulness amongst the reams of paper that contained computations that went nowhere. My cat Michchi has been my companion and my strength during this work.

I would like to acknowledge my colleagues at CFD lab Concordia, Kaveh Mohamed, Shahin Ghomeshi, Nima Tajalipour and Reza Kameshki as well as Cezary Niewiadomsky of University of Toronto and Syed Junaid Bukhari of Concordia University. It was certainly a pleasure to work with a highly talented group as this and I certainly derived a lot of inspiration out of their ideas and work.

Mr. Tingot Ngan, the proprietor of IC café on Rene Levesque, is acknowledged with much gratitude for his encouragements and support during difficult times I faced. It was Mr. Tingot's support, via employment, that I was able to finish my thesis and face the transitional time between my Masters and Doctorate. Zingee Ngan is acknowledged for making his Xeon based server available for some high-resolution computations. I am grateful for Zingee's able help in various computer related matters during the last two years.

I would like to express my deep gratitude to Dr. Rabi Baliga of McGill University for his continued support during the present work. Dr. Baliga's mentorship, both in technical matters and in life, has been instrumental in my success in postgraduate studies.

Finally, I would like to express my heartfelt gratitude for my thesis supervisor Dr. Marius Paraschivoiu. I have very much benefited from his style of supervision, which is already a legend among the graduate students. I have the deepest appreciation for his humanity as much as for his keen technical abilities. I am deeply honoured to have been his student.

Dedicated to

Moeller Family of Oakville

Klaus, Teres, Niklas, and Sabina

TABLE OF CONTENTS

LIST OF ILLUSTRATIONS

NOMENCLETURE

u^n	velocity vector field or array depending on context at time step n.
u^*	The un projected intermediate velocity obtained by solving momentum equation of Navier-Stokes equations.
$\begin{bmatrix} u_1 \\ u_2 \end{bmatrix}$	2 Dimensional velocity vector field or array depending on context
U	Total velocity array. In case of 2-D geometry, $U = \begin{bmatrix} u_1 \\ u_2 \end{bmatrix}$
q	The Pressure update parameter. Used to compute the pressure gradient term in the momentum equation of Navier-Stokes equation.
$\phi^n_{,\Delta t}$	Pressure Constraint Parameter for n^{th} time step. The solution to the Elliptic, Poisson like equation in Fractional Splitting Methods.
E	Matrix solved to obtain the Pressure constraint Parameter in *Classical* Pressure Methods
K	The stiffness matrix. The Taylor-Hood elements use bi-quadratic shape functions
K_P	The Laplace matrix used in computing the Pressure Constraint parameter *in Approximate* Pressure Method.
B	The operator indicating integration by Admas-Bashforth (AB2) Method.

β_i	$i=1,2,3$	Constants for Adams-Bashforth (AB2) integration.
β		The weight parameter on bubble functions.
D		Operator indicating integration by second order Backward Difference Formula (BDF2)
ξ_i	$i=1,2,3$	Constants for BDF2 integration, OR, Barycentric co-ordinates.
M		Mass matrix, OR, L_2 space of pressure.
M_P		Mass matrix derived from the pressure element of TH elements.
K		Stiffness Matrix (velocity elements of TH).
K_P		Stiffness Matrix (pressure elements of TH)
f_i		Forcing terms applied to NS equations.
Ω^{k_e}		The space of k^{th} element.

1. Introduction

1.1 Motivation

Incompressible flow solvers, based on Finite Element Method (FEM), face several technical challenges in terms of stability and specification of boundary conditions. The variational formulation of the Navier-Stokes (NS) equations yields the pressure as a Lagrange multiplier to a saddle point problem. Three main types of issues can be identified regarding the spatial stability of a NS solver. The type I is based on the work of Ladyzhenskaya-Babushka-Brezzi [11] who pointed out that, in order to have a stable solution, there is a necessary condition on the elements that discritize velocity and pressure. This condition is known as inf-sup condition or as LBB condition. Taylor-Hood elements (bi-quadratic in velocity and bilinear in pressure), for example, satisfy the LBB condition. Alternatively, the LBB condition can also be satisfied by adding an *artificial viscosity* or a stabilization term to the NS solver. The LBB non-compliance is manifested by spurious modes on the pressure. The type II instabilities arise in advection-dominated flow. The stabilization of the solvers to prevent oscillations at flows of high Reynolds numbers (cell Reynolds number exceeding unity by much) remains a current topic of research. This issue is tackled by adding an up winding or an artificial viscosity term to the NS solver. The type III issue of stability arises at a wall boundary, where the pressure is observed to be having a high error. This is referred to as the *numerical boundary layer* of pressure. The addition of stabilization terms is known to adversely affect the accuracy of the solutions. The presences of the type III errors are known to affect the robustness of the solvers by reducing the maximum Reynolds number of simulations.

The main motivation behind this work is the need for a robust, accurate and computationally efficient Incompressible Navier-Stokes Computational Fluid Dynamics (CFD) solver (computer code) that is based on Finite Element Method (FEM). The

elements selected for this study are the Taylor-Hood (TH) type elements and a modified Taylor-Hood element with a bubble node in the pressure (TH+Pbubble). Taylor-Hood elements are chosen primarily due to their LBB compliance and wide usage. The less known, yet promising technique of enriching the TH elements with pressure bubble nodes is also investigated. Splitting Methods (SM) that separate the solution of velocities from the pressure, are widely thought to be the best candidate for a highly computationally efficient solver. The present work, studies some of the recent state of the art splitting techniques implemented with Taylor Hood and TH+Pbubble elements. The errors related to type III stability issue are quantified. This work is directed towards a solver whose accuracy is not compromised by additional terms such as artificial viscosity while having a good robustness at high Reynolds numbers. Such solvers are in demand for current applications such as Large Eddy Simulations (LES) and Direct Numerical Simulations.

1.2 Overview of Splitting Methods

The Splitting Methods were, originally introduced by Chorin [10]. This class of solvers exploits the fact that in incompressible flow regime, the pressure does not convey any thermodynamic information and could be interpreted as a Lagrange multiplier for the incompressibility constraint, the continuity equation. This fact enables a *splitting* and separate solution of momentum and pressure/continuity equations of Navier-Stokes system via solving Helmholtz like equations and a Poission type equation respectively. There are many variations of SM reported in the literature. Based on whether the algorithm enforces the continuity by projecting the velocity fields into a solenoidal field or not, Splitting Methods can be broadly divided into two main classes of Fractional Splitting Method and Consistent Splitting Method. The Fractional Splitting Method in turn could be divided into further two classes again based on how pressure is solved. If pressure computations were based on the weak form formulation, we shall call them classical pressure computation type. If an approximation of a pressure Poisson equation was made to compute pressure, we shall call them approximate pressure solution type. Less applied velocity correction schemes are not studied in this work.

Since Chorin's original introduction in 1968, the splitting type methods have undergone a proliferation of variants. Some notable developments were the modification by Temam [37] that included a pressure like parameter in momentum equation and computing the pressure correction or *the incremental pressure* method. This was done to solve the problem of non-convergence of the pressure residue in the former method. Van Kan [41] introduced rigorous analysis of a second order accurate, incremental pressure scheme. The issue of the artificial Neumann boundary condition was tackled by Kim and Moin [28] by introducing a Dirichlet boundary condition based on the gradient of the pressure constraint parameter to the momentum equation. E and Liu introduced a novel technique based on gauge method that also was second order accurate in pressure. The approach adopted in Gauge method was also to use the boundary values in computing the gauge scalar (solution to Poisson equation) to eliminate the numerical boundary layer in the

velocity field. Here the boundary conditions on the momentum equations contain both temporal and spatial derivatives of the gauge variable ϕ.

Guermond, Minev and Shen [22] showed that the Kim and Moin method is mathematically equivalent to the Chorin-Temam method with rotational pressure update. Further, the above authors were also able to show the mathematical equivalence of the Gauge method to the Consistent Splitting Method introduced by the same authors.

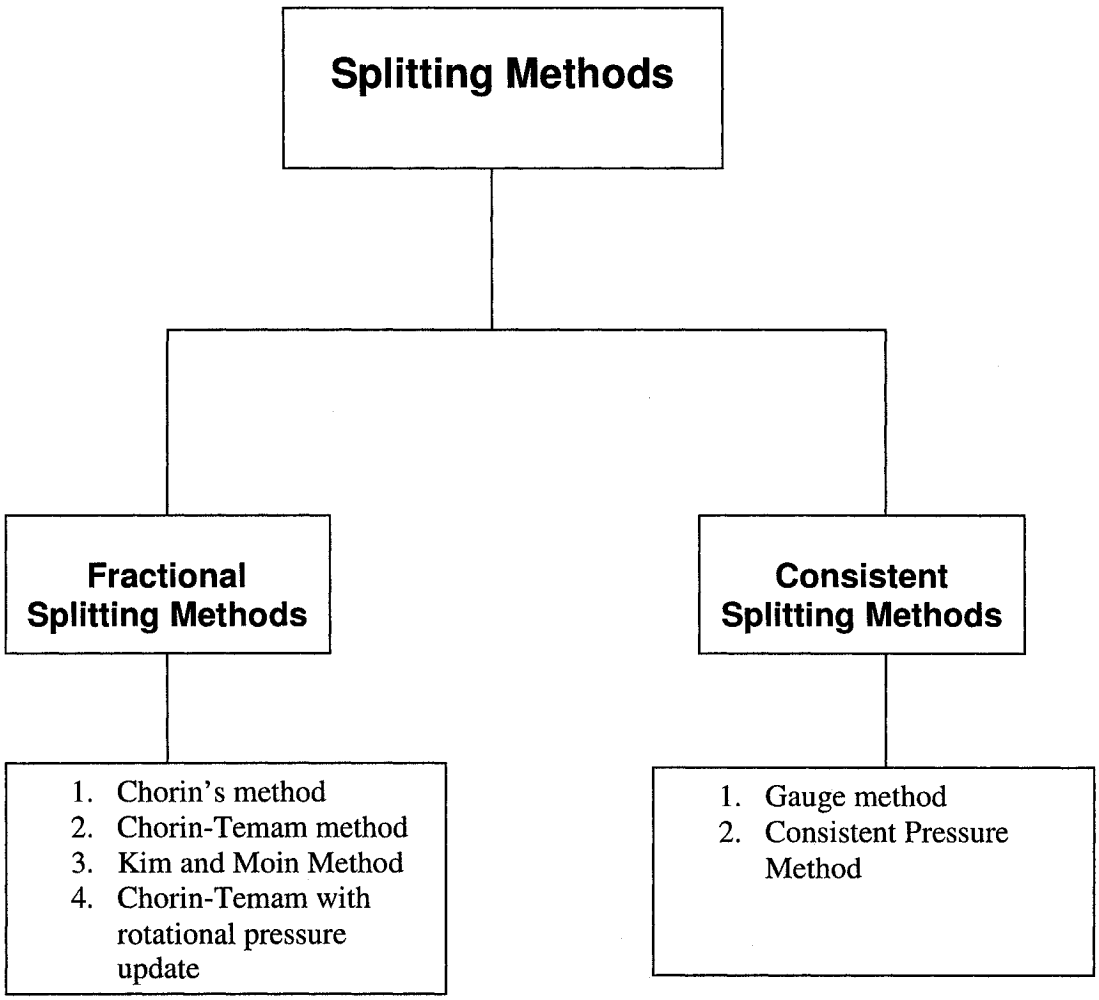

Figure 01
The basic division of the splitting method and the examples considered in the present work.

1.3 Thesis Scope

The current work studies splitting methods of pressure correction type implemented with FEM Taylor-Hood and TH+Pbubble elements. Both classes of the two main divisions of the methods, i.e., Fractional Splitting Method and Consistent Projection Method are studied. In FSM both exact pressure and approximate pressure methods are considered. The well-known *classical* methods as well as recent *cutting edge* work are presented in a unified theoretical framework using ideas and symbolism of gauge fields. The notation of gauge fields, though not always interpreted as such, were found to be particularly suitable to generalize the ideas behind each scheme and write them in a compatible manner with other methods. The present work will distinguish between the pressure update parameter q, whose gradient appear in the momentum equation, and the pressure constraint scalar ϕ, which is the solution to the pressure Poisson equation. Once each splitting method is represented in a unified symbolism and ideas, a correct classification of them as well as further insights into the workings of the algorithms is presented. The correct expression of pressure is presented. The equivalence of some of the methods will be discussed. Finally, selected representative techniques are implemented in computer codes and analyzed with the emphasis on type III spatial errors introduced in section 1.1. The matrix forms are derived for all the techniques that were computer implemented. The main issues of FEM solvers, i.e., stability, convergence and robustness are examined. The pressure boundary condition is demonstrated.

The main schemes considered in this study are: on FSM,

i) Classical Chorin-Temam method with classical pressure computation. The use of lumped mass matrix as well as a new method that uses mixed mass matrices is presented.

ii) Chorin-Temam method with approximate pressure method and rotational pressure update is investigated. By choice of a particular pressure update parameter, its equivalence with other well-known method due to Kim and Moin [22] is discussed.

Schemes considered on CSM,

i) Theoretical description of Gauge Method is presented.

ii) Guermond's consistent pressure method is presented. Its equivalence to Gauge method is discussed.

Both two-dimensional and three-dimensional computer codes of the above FSM ii) and CSM ii) methods are constructed. The effect of pressure bubbles was studied when they could be implemented in a mathematically consistent manner, namely in classical methods.

The main accomplishments of the present study are:

1. The classification of existing methods with equivalence between some of them. A general notation capable of representing each method considered is introduced.
2. A new splitting method with promising features is presented. This method is based on classical Fractional Splitting method with advantages in accuracy, computational efficiency and robustness over the original ones.
3. Properties of a novel type of element are investigated with promising results. The properties of inserting bubble nodes in the pressure elements of the Taylor-Hood elements are not widely discussed in the literature and the present work will present the effects of the bubbles on type III spatial errors.
4. The numerical boundary layer, formed by the incorrect pressure boundary condition is quantified both in terms of error in pressure and error on the continuity equation. The effect of the Taylor-Hood elements enriched with pressure bubbles on the numerical boundary layer is documented. A new finding is reported.

2. The Finite Element NS Solver

2.1 Strong and weak formulation of the Navier-Stokes Equations

The incompressible Navier-Stokes equations for homogeneous Dirichlet boundary conditions can be given by

$$\frac{\partial u}{\partial t} + (u \cdot \nabla)u + \nabla p = \nabla \cdot \left(\nu(\nabla u) + (\nabla u)^T\right) + f \quad \text{for } u(x,t) \in \Omega \qquad u\,|_{\partial\Omega} = u_b \tag{2.1}$$

$$\nabla \cdot u = 0 \qquad \text{for } u(x,t) \in \Omega \qquad u\,|_{\partial\Omega} = u_b \tag{2.2}$$

Let Ω be an open bounded domain in R^d, where d = 2 or 3 with Lipschitz continuous boundary, Γ. the velocity $u : \Omega \to R^d$, the pressure $p : \Omega \to R$ ν is the kinematic viscosity and f the bulk external force that may act on fluid body.

The first equation (2.1) is the momentum equation where the conservation of momentum of the fluid is described in the Eulerian sense. The second equation (2.2) is the continuity equation where the conservation of mass is imposed. In an incompressible flow the pressure p does not convey any thermodynamic quantities to the flow but rather acts as a Lagrange constraint to the momentum equation. This fact is also reflected in the continuity equation where there is no density term appearing in its definition. Since the momentum equation determines the pressure p only up to an additive constant, we only require $p \in L^2(\Omega)$. This becomes apparent in the following weak form formulation of the above equations.

The above equations (2.1) and (2.2) are in differential form also known as the *strong form*. The integral form or the *weak form* can be considered equivalently as well. The weak form of the equations is the starting point of the theory of Finite Element Method. The weak form equations are considered to be mathematically more general as it relaxes a few conditions required in the strong form.

In order to use the general framework of functional analysis we set the functional spaces

$$X = H_0^1(\Omega)^d, \qquad M = L_0^2(\Omega) := \{q \in L_2(\Omega)\}$$

X is composed of test or weighting function and consist of all functions which are square integrable and have square integrable first derivatives over the computational domain Ω. M is composed of square integrable functions over the domain. We now introduce the following notation:

$$-(\nabla \cdot v, \nabla \cdot u) = \int_\Omega (\nabla \cdot u) : \nu (\nabla \cdot v) dx$$

$$(v, \nabla q) = -\int_\Omega (\nabla \cdot v) q dx$$

$$(v, (u \cdot \nabla) u) = \int_\Omega v \cdot (u \cdot \nabla) u dx \tag{2.3}$$

$$(u, v) = \int_\Omega uv dx$$

The weak form formulation of the above Navier-Stokes equation are obtained by projection of the above (2.1) and (2.2) into onto the space of weight function $v \in X$ and $q \in M$ respectively.

$$(u_t, v) + (v, (u \cdot \nabla) u) + (v, \nabla p) = -(\nabla \cdot v, \nabla \cdot u) + (f, v) \tag{2.4}$$

$$-(\nabla \cdot u, q) = 0$$

Where $u_t = \dfrac{\partial u}{\partial t}$

The Finite Element domain is characterized by the discretization of the domain Ω into element domains Ω^{K_e} such that

$$\Omega = \bigcup_{e=1}^{nelem} \Omega^{k_e} \qquad \text{and} \quad \Omega^i \bigcap \Omega^j = 0 \qquad \text{for } i \neq j$$

While $\Omega^{K_e} \neq 0$ and the boundary, $\partial\Omega^{K_e}$, is piecewise smooth.

The spatial discretization of the above weak form by means of Galerkin formulation consist of defining two finite dimensional subspaces X^h, X_T^h and M^h.

$$X_T^k = \left\{ v \in H^1(\Omega) \; |v|_{\Omega^e} \in P_p(\Omega^e) \forall e \; and \quad v = 0 \, on \quad \Gamma_{wall} \right\}$$

$$X^k = \left\{ u \in H^1(\Omega) \; |v|_{\Omega^e} \in P_p(\Omega^e) \forall e \; and \quad v = u_B \, on \quad \Gamma_{wall} \right\}$$

Where P_p is the finite element interpolation space. X_T^h is the space of test function and X^h is the space of the trial functions.

In FEM the projection of (2.4) is made onto X_T^h space in each element. The solution is approximated in X^h space in each element. The interpolation functions are chosen such that they ensure the continuity across the elements ensuring a topological assembly of elements would result in solution space being in X. A co-ordinate transformation on to a barycentric co-ordinate system is introduced to generalize the computations. A topological assembly is then performed to obtain the global quantities in Ω.

2.2 Time Integration

As in the case of space, the time needs to be discretized to perform for the numerical computation. The general discrete time derivative operator could be represented by $\frac{D}{\Delta t}$ where.

$Du^* = \xi_1 u^* + \xi_2 u^n + \xi_3 u^{n-1}$ where ξ_i are factors of the integration scheme used $u^n = u(t^n)$.

In this study Backward Difference Formula of second order, BDF2, scheme is used where

$$\begin{aligned} \xi_1 &= \frac{3}{2} \\ \xi_2 &= -2 \\ \xi_3 &= \frac{1}{2} \end{aligned} \qquad (2.5)$$

Furthermore, the advection terms are integrated by B

$$Bc(u^n; u^n, v) = \beta_1 (u^n \cdot \nabla u^n, v) + \beta_2 (u^{n-1} \cdot \nabla u^{n-1}, v) + \beta_3 (u^{n-2} \cdot \nabla u^{n-2}, v)$$

The Present study uses third order Adams-Bashforth (AB3) method with

$$\begin{aligned} \beta_1 &= \frac{8}{3} \\ \beta_2 &= -\frac{7}{3} \\ \beta_3 &= \frac{2}{3} \end{aligned} \qquad (2.6)$$

The mixed method of time integration is chosen as it leads the symmetric positive definite matrices enabling a wide choice of iterative solvers including Preconditioned Conjugate Gradient solver that is used in the present work.

2.3 Taylor-Hood and Taylor-Hood/P-bubble Finite Elements

The present study concentrates on the use of Taylor-Hood (TH) elements and a lesser-known method of TH elements with bubble nodes on pressure elements. TH elements consist of second order polynomial interpolation functions for velocity and first order interpolation functions for the pressure. The elements used in the study are triangles for 2-D code and tetrahedrons for 3-D case. The bubble nodes, by their nature, are higher order.

The effect of the bubble nodes (TH+P bubble), though not widely studied, is reported in the literature [25]. The main effect of the bubbles are said to be in the imposition of the continuity condition. The present study reports on the effect of bubble nodes on continuity as well as on accuracy and robustness of the solvers.

Consider a mapping form tetrahedral element, Ω^{k_e} in global Cartesian co-ordinates $x=(x_1,x_2,x_3)$ into a reference element, $\hat{\Omega}$ whose barycentric co-ordinate system (ξ_1,ξ_2,ξ_3) is defined as

$$\xi_1=\left(\frac{vol(x,2,3,4)}{vol(1,2,3,4)}\right)$$

$$\xi_2=\left(\frac{vol(x,1,3,4)}{vol(1,2,3,4)}\right) \qquad (2.7)$$

$$\xi_3=\left(\frac{vol(x,1,2,4)}{vol(1,2,3,4)}\right)$$

$$\xi_4=\left(\frac{vol(x,1,2,3)}{vol(1,2,3,4)}\right)$$

where $vol(x,1,2,3)$ is the volume of the tetrahedron with vertices 1, 2, 3 and x.

Note that $0 \le \xi_n \le 1$ for $n = 1,2,3,4$ and $\xi_1 + \xi_2 + \xi_3 + \xi_4 = 1$.

The affine transformation of the Cartesian co-ordinates to the barycentric co-ordinates could be written as

$$\xi_\alpha = C_\alpha^{k_e} + \sum_{\beta=1}^{n} \hat{D}_{\alpha\beta}^{k_e} x_\beta \quad \text{where } \alpha = 1,2,3,4 \text{ and } n = 3 \text{ for 3-D.}$$

where

$$C_\alpha^{k_e} = \frac{-1}{\det(J)} \begin{vmatrix} x_{1_{[\alpha+1]}} & x_{2_{[\alpha+1]}} & x_{3_{[\alpha+1]}} \\ x_{1_{[\alpha+2]}} & x_{2_{[\alpha+2]}} & x_{3_{[\alpha+2]}} \\ x_{1_{[\alpha+3]}} & x_{2_{[\alpha+3]}} & x_{3_{[\alpha+3]}} \end{vmatrix}$$

$$\hat{D}_{\alpha 1}^{k_e} = \frac{(-1)^{\alpha+1}}{\det(J)} \begin{vmatrix} 1 & x_{2_{[\alpha+1]}} & x_{3_{[\alpha+1]}} \\ 1 & x_{2_{[\alpha+2]}} & x_{3_{[\alpha+2]}} \\ 1 & x_{2_{[\alpha+3]}} & x_{3_{[\alpha+3]}} \end{vmatrix}$$

$$\hat{D}_{\alpha 2}^{k_e} = \frac{(-1)^{\alpha+1}}{\det(J)} \begin{vmatrix} x_{1_{[\alpha+1]}} & 1 & x_{3_{[\alpha+1]}} \\ x_{1_{[\alpha+2]}} & 1 & x_{3_{[\alpha+2]}} \\ x_{1_{[\alpha+3]}} & 1 & x_{3_{[\alpha+3]}} \end{vmatrix} \qquad (2.8)$$

$$\hat{D}_{\alpha 3}^{k_e} = \frac{(-1)^{\alpha+1}}{\det(J)} \begin{vmatrix} x_{1_{[\alpha+1]}} & x_{2_{[\alpha+1]}} & 1 \\ x_{1_{[\alpha+2]}} & x_{2_{[\alpha+2]}} & 1 \\ x_{1_{[\alpha+3]}} & x_{2_{[\alpha+3]}} & 1 \end{vmatrix}$$

where $[\alpha] = \alpha_{\bmod 4}$ and $x_{i_{[\alpha]}}$ is the co-ordinate of the local node α of the element Ω^{k_e} in i co-ordinate.

The co-ordinate transformation to barycentric to natural co-ordinates could now be given by

$$x_\beta = \left(\hat{D}^{k_e}_{\alpha\beta}\right)^{-1}\xi_\alpha - \left(\hat{D}^{k_e}_{\alpha\beta}\right)^{-1}C^{k_e}_{\alpha} \qquad \alpha = 1,..,3, \quad \beta = 1,..,3. \tag{2.9}$$

Note that the last row of C^{k_e} and $\hat{D}^{k_e}$ has been excluded since ξ_4 is not an independent variable.

The Jacobian of the transformations (determinant of it) is given by

$$\det(J) = |J| = \det\left(\hat{D}^{k_e}\right)^{-1}. \tag{2.10}$$

For transformation

$$x = \sum_{\alpha=1}^{4} \hat{x}^{k_e}_{\alpha}\xi_\alpha \tag{2.11}$$

where $x^{k_e}_{\alpha}$ is the position vector of local node α of element Ω^{k_e}

The elemental basis functions for $h_\alpha(\xi_1,\xi_2,\xi_3)$, $\alpha = 1,...,4$ for linear P_1 tetrahedron elements are

In 2D P_1+P bubble

$$h_1 = \xi_1$$
$$h_2 = \xi_2 \qquad (2.12)$$
$$h_3 = 1-\xi_1-\xi_2$$

and the bubble element

$$h_B = \beta\xi_1\xi_2(1-\xi_1-\xi_2)$$

Where β is a parameter that could be adjusted to facilitate a desired solution process. Smaller β leads to ill-conditioned matrices to be solved to obtain pressure.

In 3D P_1+P bubble

$$h_1 = \xi_1$$
$$h_2 = \xi_2$$
$$h_3 = \xi_3 \qquad (2.13)$$
$$h_4 = 1-\xi_1-\xi_2-\xi_3$$

the bubble function is

$$h_B = \beta\xi_1\xi_2\xi_3(1-\xi_1-\xi_2-\xi_3)$$

The second order basis functions can be derived for tetrahedrons with mid-point nodes on the edges. The local elemental basis functions in bayricentric co-ordinates are

2D P_2 interpolation function

$$
\begin{aligned}
h_1 &= \xi_1(-1+2\xi_1) \\
h_2 &= \xi_2(-1+2\xi_2) \\
h_3 &= (1-\xi_1-\xi_2)(1-2\xi_1-2\xi_2) \\
h_4 &= 4\xi_1\xi_2 \\
h_5 &= 4\xi_2(1-\xi_1-\xi_2) \\
h_6 &= 4\xi_1(1-\xi_1-\xi_2)
\end{aligned}
\qquad (2.14)
$$

In 3D P_2 interpolation function

$$
\begin{aligned}
h_1 &= (2\xi_1-1)\xi_1 \\
h_2 &= (2\xi_2-1)\xi_2 \\
h_3 &= (2\xi_3-1)\xi_3 \\
h_4 &= (2\xi_4-1)\xi_4 \\
h_5 &= 4\xi_1\xi_2 \\
h_6 &= 4\xi_2\xi_3 \\
h_7 &= 4\xi_1\xi_3 \\
h_8 &= 4\xi_1\xi_4 \\
h_9 &= 4\xi_2\xi_4 \\
h_{10} &= 4\xi_3\xi_4
\end{aligned}
\qquad (2.14)
$$

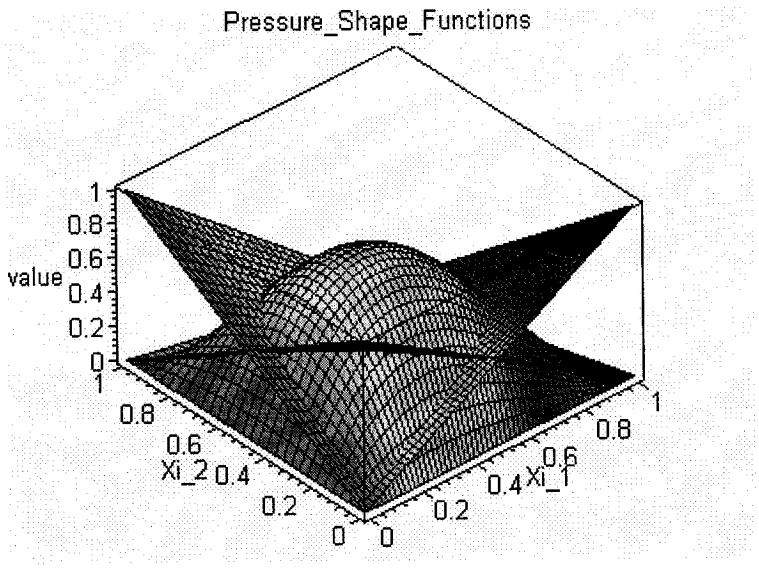

Figure 02
2D pressure shape functions of the Taylor-Hood element with the bubble. Note that the bubble function is scaled by $\beta = 27$ to bring it to the same scale as the bilinear shape functions.

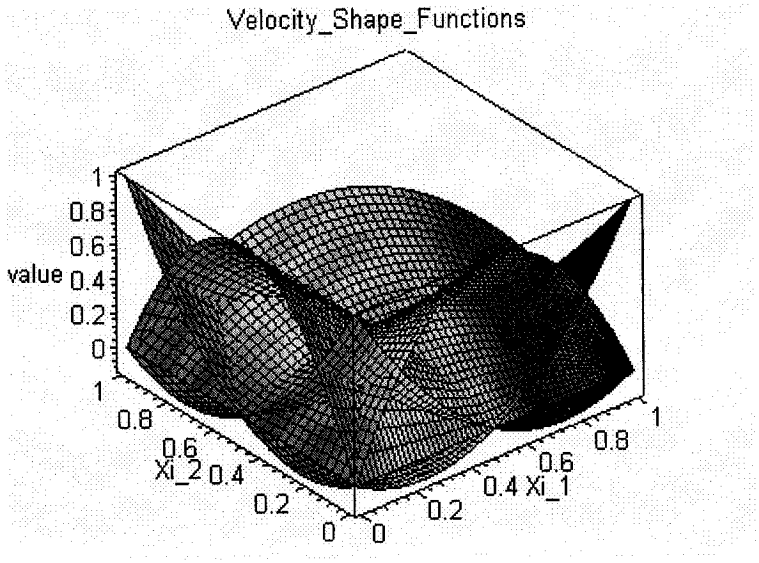

Figure 03
2D velocity shape functions of Taylor-Hood elements.

2.4 Matrix assembly and Navier-Stokes system in matrix form

With the elements defined, the matrix equivalents of the weak form operators in equations (2.3) can be obtained for each element.

The elemental stiffness matrix is derived as below

$$A_{\alpha\beta}^{k_e} = |J| \sum_{m=1}^{3} \sum_{n=1}^{3} \sum_{n'}^{3} \hat{D}_{nm}^{k_e} \hat{D}_{n'm}^{k_e} G_{\alpha\beta nn'} \tag{2.15}$$

where

$\hat{D}_{nm}^{k_e} = \dfrac{\partial \xi_n}{\partial x_m}$ as defined in equation (2.8)

and $G_{\alpha\beta nn'}$ is defined below

$$G_{\alpha\beta nn'} = \int_0^1 \int_0^{1-\xi_3} \int_0^{1-\xi_2-\xi_3} \frac{\partial h_\alpha}{\partial \xi_n} \frac{\partial h_\beta}{\partial \xi_{n'}} d\xi_1 d\xi_2 d\xi_3 \tag{2.16}$$

The elemental mass matrix is given by

$$M_{\alpha\beta}^{k_e} = \int_0^1 \int_0^{1-\xi_2} \int_0^{1-\xi_2-\xi_3} h_\alpha h_\beta |J| d\xi_1 d\xi_2 d\xi_3 \tag{2.17}$$

Where

$|J|$ is given by (2.10)

The elemental pressure constraint matrix is given by

$$D^{k_e}_{1\alpha\beta} = |J|\sum_{n=1}^{3} \hat{D}^{k_e}_{n1} H_{\alpha\beta n'}$$

$$D^{k_e}_{2\alpha\beta} = |J|\sum_{n=1}^{3} \hat{D}^{k_e}_{n2} H_{\alpha\beta n'} \qquad (2.18)$$

$$D^{k_e}_{3\alpha\beta} = |J|\sum_{n=1}^{3} \hat{D}^{k_e}_{n3} H_{\alpha\beta n'}$$

$$H_{\alpha\beta n'} = \int_0^1 \int_0^{1-\xi_3} \int_0^{1-\xi_2-\xi_3} \frac{\partial h_\alpha}{\partial \xi_{n'}} g_\beta d\xi_1 d\xi_2 d\xi_3 \qquad (2.19)$$

where $\alpha = 1,..,10$ and $\beta = 1,..,4$ for the 3D TH elements and $\alpha = 1,..,10$ and $\beta = 1,..,5$ for the TH+bubble .

In 2D $\alpha = 1,..,6$ and $\beta = 1,..,3$ for the 2D TH elements and $\alpha = 1,..,6$ and $\beta = 1,..,4$ for the TH+bubble.

Similarly for the advection term

$$C^{k_e}_{1\alpha\beta\gamma} = |J|\sum_{n=1}^{3} \hat{D}^{k_e}_{n1} C^{k_e}_{\alpha\beta n\gamma}$$

$$C^{k_e}_{2\alpha\beta\gamma} = |J|\sum_{n=1}^{3} \hat{D}^{k_e}_{n2} C^{k_e}_{\alpha\beta n\gamma} \qquad (2.20)$$

$$C^{k_e}_{3\alpha\beta\gamma} = |J|\sum_{n=1}^{3} \hat{D}^{k_e}_{n3} C^{k_e}_{\alpha\beta n\gamma}$$

$$C^{k_e}_{\alpha\beta n\gamma} = \int_0^1 \int_0^{1-\xi_3} \int_0^{1-\xi_2-\xi_3} h_\alpha h_\beta \frac{\partial h_\gamma}{\partial \xi_n} d\xi_1 d\xi_2 d\xi_3 \qquad (2.21)$$

Comment 01: Note that the above *pressure constraint* matrix is where the bubble nodes play a role. The bubble nodes are not typical normalized nodes on an element but that of a *"floating"* nature. The weight of the bubble nodes could be adjusted by the scalar parameter β. The solution of the pressure constraint parameter, ϕ, obtained at the bubble nodes are generally not continuous with the solution obtained at other nodes. The solution *floats* and depends on the value of β. The adjustment of the β parameter through the domain could be considered as a P-adaptation where the mesh stays the same and the order of the interpolation function changes (See Lohner)[15]. The present work does not consider the solutions of pressure obtained for bubble nodes but bubbles are used as a device to improve continuity constraint.

The global matrices are obtained by assembling the elemental matrices. Assembly operator $\mathbf{A}$ creates the global matrices corresponding to the domain Ω by performing a topological assembly. For example the global mass matrix is given by

$$M = \mathbf{A}^{e} M^{k_e} \tag{2.22}$$

The global mass matrix corresponding to two spatial dimension space is defined by

$$\overline{M} = \begin{bmatrix} M & 0 \\ 0 & M \end{bmatrix} \tag{2.23}$$

And similarly for other matrices.

The matrix for of the weak form in equations (2.4) could now be written as

$$\overline{M}U_t + \overline{C}(\overline{u})U + \overline{D}P = -\overline{K}U + \overline{M}F \tag{2.24}$$

$$\overline{B}U = 0$$

The Cartesian 2-dimentional form of the above matrix form can be written as

$$\begin{bmatrix} M & 0 \\ 0 & M \end{bmatrix}\begin{bmatrix} u_{1,t} \\ u_{2,t} \end{bmatrix}+\begin{bmatrix} C(u_1,u_2) & 0 \\ 0 & C(u_1,u_2) \end{bmatrix}\begin{bmatrix} u_1 \\ u_2 \end{bmatrix}+\begin{bmatrix} D_1 & 0 \\ 0 & D_2 \end{bmatrix}\begin{bmatrix} p \\ p \end{bmatrix}=-\begin{bmatrix} K & 0 \\ 0 & K \end{bmatrix}\begin{bmatrix} u_2 \\ u_1 \end{bmatrix}+\begin{bmatrix} M & 0 \\ 0 & M \end{bmatrix}\begin{bmatrix} f_x \\ f_y \end{bmatrix}$$

$$\begin{bmatrix} B_1 & B_2 \end{bmatrix}\cdot\begin{bmatrix} u_1 \\ u_2 \end{bmatrix}=0 \qquad \text{With boundary conditions} \qquad (2.25)$$

When solving equations (2.25) numerically, a well-known technical difficulty is encountered. The problem arises form the fact that no explicit mathematical expression of the time evolution of the pressure is possible. This leads to additional, and often artificial, boundary conditions that are either explicitly or implicitly imposed on pressure. Let us examine this fact further by taking the divergence of the momentum equation; this leads to the pressure-Poisson equation

$$\nabla^2 p = -\nabla\cdot(u\cdot\nabla u) \qquad (2.26)$$

The natural boundary condition for solving the above, obtained from the momentum equation, is

$$\frac{\partial p}{\partial n} = n\cdot(\nabla\nu\nabla u)\Big|_{\partial\Omega}. \qquad (2.27)$$

The above is an elliptic Poisson equation with Neumann boundary condition. This involves evaluating the viscous term at the boundary. A consistent method of solving the pressure Poisson equation in a given discretization remains a difficult problem. Methods, such as direct solution of above matrix equation, make an implicit, incorrect boundary condition on pressure. It is clear from above that Dirichlet velocity boundary condition alone is not sufficient to correctly enforce the correct Neumann type boundary condition on pressure. The resulting error leads to a numerical boundary layer near the wall boundaries.

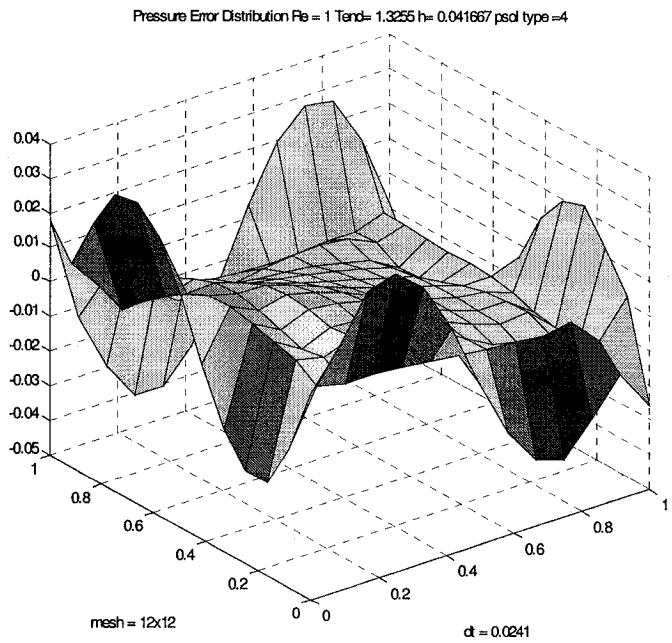

Figure 04
The error in pressure solution computed using an exact solution (see section 5.2) to Navier-Stokes equations

The solution process of the above two systems of equations, via single (see equation 3.39) matrix representation is know to be slow. There are various schemes proposed in the literature ranging from a direct solve of the global matrix equation to Uzawa[5][12][16][37] type iterative solvers. All of the reported iterative algorithms, so far, are know to be slow in convergence. This fact, along with the large size of the global matrix, makes the solution process computationally expensive. The slow convergence of the pressure elliptic problem is identified to be the main cause behind iterative solver needing more work. Decoupling and solving the pressure elliptic equation separately would facilitate a computationally reduced method.

The Splitting type methods are currently thought to be the best candidate to solve both issues of boundary condition and slow convergence/high expenses.

3. Fractional Splitting Method

3.1 Theoretical framework of Splitting Methods

The basic principle of Splitting methods is to compute the velocity and pressure fields in separate steps. The velocity and pressure computations are linked via an intermediate velocity computed by solving the momentum equations. This intermediate velocity solution is then used to compute a constraint scalar. In projection schemes the intermediate velocity is then projected to a solenoidal (divergence free) vector field via the computed pressure-like constraint scalar (see Temam [37]). The theoretical basis of the splitting/projection, we shall call them Fractional *Splitting Methods*, is the theorem of orthogonal decomposition due to Ladyzhenskaya (1969), which is based on Hodge-Helmholtz decomposition principle, which states smooth vector fields can be decomposed into rotational and solenoidal components.

The theorem states that any vector field u^* in Ω admits a unique orthogonal decomposition

$$u^* = u + \nabla\phi \tag{3.1}$$

where u is a solenoidal vector field with zero normal component on the boundary, i.e., $\nabla \cdot u = 0$ and $n \cdot u = 0$ on $\partial\Omega$ and ϕ is a scalar function (call it *constraint scalar*). Neither u^* nor ϕ is unique (See Chorin-the text book)[11].

The vectors u and $\nabla\phi$ are orthogonal in function space:

$$(u, \nabla\phi) = \int u \cdot \nabla\phi \, dx \quad = -\int (\nabla \cdot u)\phi \, dx \quad = 0 . \tag{3.2}$$

The general approach to Fractional Splitting schemes is to use the following approximation to the momentum equation.

$$\frac{\partial u^*}{\partial t} + (u \cdot \nabla)u + \nabla q = \nabla \nu \nabla u^* \tag{3.4}$$

where ∇q is the pressure gradient approximation. In some Fractional Splitting methods it can be zero (e.g. see Chorin method below). In others, it is a simple or combination of lagging constraint scalar ϕ. We shall call q the *Pressure Parameter.*

The u^* solution is advanced for some time interval $t_i \le t \le t_{i+1}$ and then projected to a solenoidal vector field u. This is done via the Helmholtz-Hodge decomposition (3.1). In order to use this equation for the purpose of projection, one still needs the scalar ϕ. By taking the divergence of (3.1) and continuity (2.2) we obtain,

$$\nabla^2 \phi = \nabla \cdot u^* \tag{3.5}$$

The solution of the above elliptic constraint equation will allow the projection of the solution to the approximate momentum equation (3.4) i.e., u^* to a solenoidal vector field of u.

The correct pressure, at any time step, can be obtained by substituting u^* in (3.1) to the approximate momentum equation (3.4).

$$\frac{\partial (u + \nabla \phi)}{\partial t} + (u \cdot \nabla)u + \nabla q = \nabla \nu \nabla (u + \nabla \phi) \tag{3.6}$$

After a simple manipulation, we obtain

$$\nabla p = \nabla(q + \phi_t) + \nabla \nu \nabla(\nabla \phi) \tag{3.7}$$

or

$$p = q + \phi_t + \nu \nabla(\nabla \phi) \text{ up to a constant.} \tag{3.8}$$

In the present work, we shall keep a separate label q for the pressure update term instead of more common p. We shall do so without any loss of generality. From the above relation (3.8), it is clear, that the total information about pressure is contained in both q and in u^* via $\nabla \phi$. Now a general formula for pressure parameter update that are used in splitting/projection methods can be presented as

$$q^{n+1} = q^n + L_1(\phi^{n+1}) \text{ and updating formula}$$

$$q^* = L_2(q^{n+1}, q^n). \tag{3.9}$$

Where L_1 and L_2 are general functions to be proposed for updating the pressure like parameter each time iteration. We shall investigate four methods of updating the pressure like parameter that are commonly reported in the literature.

The present work considers the explicit integration of the advection term, $(u \cdot \nabla)u$. We also choose the projected vector field, u to compute the advection terms. In light of the success of non-projected methods we recognize that the use of u^* is also justified in using to compute the advection term. In approximate pressure methods, u^* has the advantage of not having the numerical boundary layer where as u satisfies continuity equation better.

The existing methods and the method to be proposed in Section 3.5.2 (Mixed Mass Method) could now be analysed using the notation of pressure parameter q and pressure constraint parameter ϕ.

3.2 Chorin's Method

The following scheme, originally proposed by Chorin in 1968[10] marks the beginning of the splitting/projection type methods. The method has been implemented repeatedly in Finite Difference Method, Finite Volume Method, Finite Element Method and Spectral Methods. The fact that the residual of the pressure constraint scalar ϕ (Note that in this case the pressure parameter is zero) does not vanish as solution approaches a steady state was in the past considered to be a negative aspect of the method.

We shall use a symbolic representation of the algorithm using a first order time integration for clarity without loss of generality.

3.2.1 General Algorithm of Chorin's method

(a) Adjective/Diffusive prediction: $u^n \rightarrow u^*$

$$\left[\frac{1}{\Delta t} - \nabla \nu \nabla\right] \cdot \left(u^* - u^n\right) + \left((u \cdot \nabla) u\right)^{*,n+1} = \nabla \nu \nabla u^n \tag{3.10}$$

*The superscript *outside the bracket for the advection term means that advection term is evaluated appropriately with an integration scheme such as the one described in Section 2.2.*

Note that there is no q update as q is not used in the momentum equation.

(b) Pressure Constraint Scalar

Solving the system

$$\begin{cases} \nabla \cdot u^{n+1} = 0 \\ \dfrac{u^{n+1} - u^*}{\Delta t} + \nabla \phi_{,\Delta t}^{n+1} = 0 \end{cases} \tag{3.11}$$

where $\dfrac{\phi}{\Delta t} = \phi_{,\Delta t}$

Above two equations lead to solving:

$$\nabla^2 \phi_{,\Delta t}^{n+1} = \frac{\nabla \cdot u^*}{\Delta t} \tag{3.12}$$

(c) Velocity correction

$$u^{n+1} = u^* - \Delta t \nabla \phi_{,\Delta t}^{n+1} \tag{3.13}$$

The Chorin Method is a *pressure free* method where the pressure-like parameter does not appear in the momentum equation. There are several advantages to this type of method. We make the observation that the numerical boundary layer (the error in the solution near the walls) does not accumulate in the pressure like parameter in this type of method. In that respect, the method is similar to Kim and Moin method described below. Previous work refers to the pressure constraint parameter $\phi_{,\Delta t}$ as pressure. It is clear from equation (3.8) that it is not the case and the non-convergence of the pressure constraint parameter is what is reported in the literature [11][15][37]. Present author speculates that non – uniqueness of $\phi_{,\Delta t}$ as a possible cause of the oscillations. By inserting a pressure

parameter, q into the momentum equation and computing a correction term for $\phi_{,\Delta t}$, the oscillations in the residual are removed.

3.3 Chorin-Temam Method

The issue of the non-convergent pressure of the original Chorin method was solved by introducing a pressure parameter into the momentum equation. Consequently, the approximate pressure parameter computation is now replaced by the computation of the pressure parameter difference, dq, for the lagging parameter to obtain the new update. This is sometimes referred to as an incremental pressure method.

3.3.1 General Algorithm of Chorin-Temam Method

(a) *Advection/Diffusive prediction* $u^n \rightarrow u^*$*:*

$$\left[\frac{1}{\Delta t} - \nabla \nu \nabla\right] \cdot \left(u^* - u^n\right) + \left((u \cdot \nabla)u\right)^{*,n+1} + \nabla q^{*,n+1} = \nabla \nu \nabla u^n \tag{3.14}$$

(b) Pressure Constraint Scalar

By solving the system

$$\begin{cases} \nabla \cdot u^{n+1} & = 0 \\ \dfrac{u^{n+1} - u^*}{\Delta t} + \nabla\left(q^{n+1} - q^{*,n+1}\right) & = 0 \end{cases} \tag{3.15}$$

Where $q^{n+1} - q^{*,n+1} = \phi_{,\Delta t}^{n+1}$

Type I q update equation.

$q^{*,n+2} = q^{*,n+1} + \phi_{,\Delta t}^{n+1}$

Type II q update equation.

$$q^{n+1} = q^{*,n+1} + \phi_{,\Delta t}^{n+1}$$

$$q^{*,n+2} = 2q^{n+1} - q^{n} \tag{3.16}$$

Type III q update equation.

$$q^{*,n+2} = q^{*,n+1} + \phi_{,\Delta t}^{n+1} - \nu\nabla \cdot u^{*}$$

Type IV q update equation.

$$q^{n+1} = q^{*,n+1} + \phi_{,\Delta t}^{n+1} - \nu\nabla \cdot u^{*}$$

$$q^{*,n+2} = 2q^{n+1} - q^{n}$$

Note: From equation (3.1) and continuity, equation (2.2), that $\nabla \cdot u^{*} = \nabla \cdot (u + \nabla\phi) = \nabla^{2}\phi$

***Comment 02**: Collapsing (summing) the momentum equation (3.14) and pressure projection equation (3.15) motivates the* $\nu\nabla \cdot u^{*}$ *term in type III and IV pressure updates. In other words the rotational term is required for the system to be consistent. We shall discuss this point further in the weak form formulation below. The discretization of the time derivative of the constraint scalar* $\phi_{,t}$ *is considered in most recent work of Guermond et. al. in November 2005 [21].*

The above two equations lead to solving:

$$\nabla^{2}\phi_{,\Delta t}^{n+1} = \frac{\nabla \cdot u^{*}}{\Delta t} \tag{3.17}$$

The weak form derivation of equation (3.17) has two distinct alternate forms, Classical and Approximate Pressure. This will be discussed in section 3.2.2.

(d) Velocity correction

$$u^{n+1} = u^* - \Delta t \nabla \phi^{n+1}_{,\Delta t}$$

This method forms the basis for modern Fractional Splitting type methods. Based on how pressure is computed in the weak form, the above general algorithm splits into approximate and classical pressure computation methods. The four pressure update methods further generalize the method. The original Chorin-Temam method is an approximate pressure computation with type I pressure update. The rotational pressure update methods, type III and IV are more recent development [7][22][23][24].

3.3.2 Weak form of Splitting Algorithms

The weak form for the Chorin-Temam equation is studied below. The implementation of the weak form can be conducted in two distinct ways, namely, the *classical splitting method* and the *approximate pressure* method. The difference between the two methods stems from the different implementations of the pressure-Poisson equation.

(a) Adjective/Diffusive prediction: $u^n \rightarrow u^*$

$$\left(\frac{Du^*}{\Delta t}, v\right) + B\left(u^n \cdot \nabla u^n, v\right) - \left(q^n, \nabla \cdot v\right) = \left(\nabla \nu \nabla u^*, v\right) \qquad u\,|_{\partial\Omega} = u_b \qquad \forall v \in X \tag{3.18}$$

Where D *and* B *are time integration described in Section 2.2*

(b) Pressure Constraint Scalar: solve for ϕ *using the Hodge-Helmholtz decomposition and continuity equation.*

$$\left(\nabla \cdot u^n, q\right) = 0 \qquad u\,|_{\partial\Omega} = u_b \quad \forall q \in M \tag{3.19}$$

$$\left(\frac{u^{n+1} - u^*}{\Delta t}, v\right) + \left(\phi_{,\Delta t}, \nabla \cdot v\right) = 0 \qquad u\,|_{\partial\Omega} = u_b \quad \forall v \in X \tag{3.20}$$

The Classical Splitting methods solve (3.19) and (3.20).
The Approximate Pressure methods will solve a weak form equivalent to (3.17)

$$\left(\nabla \phi^{n+1}_{,\Delta t}, \nabla \varphi\right) = -\frac{\xi_1}{\Delta t}\left(\nabla \cdot u^*, \varphi\right) \qquad u^*\,|_{\partial\Omega} = u_b \; \forall \varphi \in M \tag{3.21}$$

where ξ_1 *is the first constant of the integration scheme. In the present study it is BDF2.*

Four update schemes for the pressure are considered in this work.

Type I

$$\left(q^{*,n+2},\varphi\right)=\left(q^{*,n+1}+\phi_{,\Delta t}^{n+1},\varphi\right) \tag{3.22}$$

Type II

$$\left(q^{n+1},\varphi\right)=\left(q^{*,n+1}+\phi_{,\Delta t}^{n+1},\varphi\right) \tag{3.23}$$

And

$$q^{*,n+2}=2q^{n+1}-q^{n}$$

Type III

$$\left(q^{*,n+2},\varphi\right)=\left(q^{*,n+1}+\phi_{,\Delta t}^{n+1}-\nu\nabla\cdot u^{*},\varphi\right) \tag{3.24}$$

Type IV

$$\left(q^{n+1},\varphi\right)=\left(q^{*,n+1}+\phi_{,\Delta t}^{n+1}-\nu\nabla\cdot u^{*},\varphi\right) \tag{3.25}$$

And

$$q^{*,n+2}=2q^{n+1}-q^{n}$$

3.3.3 On rotational pressure update

The motivation behind the type III and IV pressure update formula could be seen by first, testing the momentum equation(s) by a scalar gradient

$$\left(\frac{Du^*}{\Delta t},\nabla\varphi\right)+B\left(u^n\cdot\nabla u^n,\nabla\varphi\right)+\left(\nabla q^{*,n+1},\nabla\varphi\right)=\left(\nu\nabla\nabla\cdot u^*-\nu\nabla\times\nabla\times u^*,\nabla\varphi\right) \tag{3.26}$$

$$\left(\nabla\phi^{n+1}_{,\Delta t},\nabla\varphi\right)=\frac{\xi_1}{\Delta t}\left(u^*,\nabla\varphi\right) \tag{3.27}$$

Note $\left(\nabla\times\nabla\times u^*,\nabla\varphi\right)=0$ (3.28)

Simple collapse (by summing the equations) of equations (3.26) and (3.27) and separating the pressure parameter terms, we obtain

$$\left(\nabla q^{*,n+2},\nabla\varphi\right)=\left(\nabla q^{*,n+1}+\nabla\phi^{n+1}_{,\Delta t}-\nabla\nu\nabla\cdot u^*,\nabla\varphi\right) \tag{3.29}$$

The above equation is in H^1 norm. The equality holds for L^2 norm i.e., projecting onto φ instead of $\nabla\varphi$

$$\left(q^{n+2},\varphi\right)=\left(q^n+\phi^{n+1}_{,\Delta t}-\nu\nabla\cdot u^*,\varphi\right) \tag{3.30}$$

In the projection step the pressure constraint scalar, $\phi^{n+1}_{,\Delta t}$ is supposed to live in H^1 space while satisfying Neumann boundary conditions but when computing the update for the pressure parameter, q^{n+1} both are in L^2 space. The discritization of both are also to be done with two different discrete spaces such that they comply with LBB criteria for stability.

The matrix version of the above involves the "pressure mass matrix" based on the shape functions of the elements used in pressure computations.

3.4 Kim and Moin Scheme

Kim and Moin recognized the difficulties associated with imposing the correct pressure boundary condition and dealing with the so-called discretization error. Their solution was to use the gradient of the constraint scalar $\nabla\phi|_\Gamma$ as the boundary value when solving the Helmholtz equation for the unprojected initial velocity u^*. The lagging time constraint scalar was used for the computation of the gradient. This enabled the cancellation of the errors at the walls from projected velocity u as $\left(u^* - \nabla\phi\right)\big|_\Gamma = 0$

We shall present this method as a sub topic of the Chorin-Temam method based on the work by Guremond, Minev and Shen [22]. The above authors were able to show that the method originally proposed by Kim and Moin is in fact equivalent to the Chorin-Temam method with a rotational form of the pressure update, types III or IV.

The method has been called pressure-free and in this respect, resembles the original Chorin method. Kim and Moin recognised the advantages of the pressure-free method as it avoids accumulating error in the pressure term. It has been shown that the above boundary condition is a sufficient condition for the second order accuracy.

The weak form of the algorithm of Kim and Moin Scheme could be presented as below.

$$\frac{1}{\Delta t}\left(\xi_1 u^* + \sum_{i=2}^{3} \xi_i u^{n+2-i}\right) - \nu\nabla^2 \hat{u}^{n+1} = g\left(t^{n+1}\right) \text{ with boundary condition } u^*\big|_\Gamma = \frac{\Delta t}{\xi_1}\nabla\phi^{*,n+1}\Big|_\Gamma$$

$$\begin{cases} \dfrac{\xi_1}{\Delta t}\left(u^{n+1} - u^*\right) + \nabla\phi^{n+1} = 0 \\ \nabla\cdot u^{n+1} = 0, \qquad u^{n+1}\cdot n\big|_\Gamma = 0 \end{cases}$$

$$\phi^{*,n+1} = \begin{cases} 0 & if \quad r = 0 \\ \phi^n & if \quad r = 1 \\ 2\phi^n - \phi^{n-1} & if \quad r = 2 \end{cases} \text{ where } r \text{ is the order of the integration scheme used}$$

3.5 Matrix forms of Fractional Splitting Methods

The matrix representation of the Chorin-Temam method is presented below. Without the loss of generality, we present the 2-dimentional cases. Three alternative methods of classical splitting methods (that solves the matrix version of equations (3.19) and (3.20)) and one approximate pressure method (solves the matrix version equation (3.21)) is presented.

3.5.1 Solution Algorithm in Matrix form

(a) Adjective/Diffusive prediction: $U^n \rightarrow U^*$

$$\left(\overline{K}+\frac{\xi_1}{\Delta t}\overline{M}\right)U^* = -\frac{\overline{M}}{\Delta t}\left(\xi_2 U^n + \xi_3 U^{n-1}\right) + \overline{D}Q^* + \left(\beta_1 C\left(U^n\right)U^n + \beta_2 C\left(U^{n-1}\right)U^{n-1} + \beta_3 C\left(U^{n-1}\right)U^{n-2}\right) + \overline{M}F^{n+1} \tag{3.31}$$

In 2D we could write above equations as

$$\begin{bmatrix} K+\frac{\xi_1}{\Delta t}M & 0 \\ 0 & K+\frac{\xi_1}{\Delta t}M \end{bmatrix}\begin{bmatrix} u_1^* \\ u_2^* \end{bmatrix} = -\begin{bmatrix} \frac{M}{\Delta t}\left(\xi_1 u_1^{n-1} + \xi_1 u_1^{n-2}\right) & 0 \\ 0 & \frac{M}{\Delta t}\left(\xi_1 u_2^{n-1} + \xi_1 u_2^{n-2}\right) \end{bmatrix} + \begin{bmatrix} D_1^T & 0 \\ 0 & D_2^T \end{bmatrix}\begin{bmatrix} q^{*,n+1} \\ q^{*,n+1} \end{bmatrix}$$
$$+ \begin{bmatrix} \beta_1 C\left(U^n\right)u_1^n + \beta_2 C\left(U^{n-1}\right)u_1^{n-1} + \beta_3 C\left(U^{n-2}\right)u_1^{n-2} & 0 \\ 0 & \beta_1 C\left(U^n\right)u_2^n + \beta_1 C\left(U^{n-1}\right)u_2^{n-1} + \beta_1 C\left(U^{n-2}\right)u_2^{n-2} \end{bmatrix} +$$
$$+ \begin{bmatrix} M & 0 \\ 0 & M \end{bmatrix}\begin{bmatrix} f_1^{n+1} \\ f_2^{n+1} \end{bmatrix} \tag{3.32}$$

And the continuity equation is given by

$$[D_1, D_2]\begin{bmatrix} u_1 \\ u_2 \end{bmatrix} = 0 \tag{3.33}$$

The Dirichlet boundary conditions are imposed by removing corresponding rows and columns from the vectors and matrices and building a RHS vector that is the matrix boundary value vector multiplication. Note also that if the original Chorin method were considered, the pressure parameter term in the momentum equation would not exist.

$$In\ 2D\ case\ U=\begin{bmatrix}u_1\\u_2\end{bmatrix}\ and\ \overline{D}=\begin{bmatrix}D_1 & 0\\0 & D_2\end{bmatrix}$$

The resulting Helmholtz type matrix is symmetric and the Conjugate Gradient (CG) method could be used to solve it

(b) Pressure Constraint Scalar:

1-Classical methods

The Classical methods solve the matrix form of continuity (3.19) and pressure scalar equations (3.20). The matrix form is obtained as below

$$\begin{bmatrix}M & 0\\0 & M\end{bmatrix}\begin{bmatrix}u_1^{n+1}\\u_2^{n+1}\end{bmatrix}-\begin{bmatrix}M & 0\\0 & M\end{bmatrix}\begin{bmatrix}u_1^{*}\\u_2^{*}\end{bmatrix}=\frac{\Delta t}{\xi_1}\begin{bmatrix}D_1^T & 0\\0 & D_2^T\end{bmatrix}\begin{bmatrix}\phi_{,\Delta t}^{n+1}\\\phi_{,\Delta t}^{n+1}\end{bmatrix} \qquad (3.34)$$

Moving the Mass matrix to RHS in the above we get

$$\begin{bmatrix}u_1^{n+1}\\u_2^{n+1}\end{bmatrix}-\begin{bmatrix}u_1^{*}\\u_2^{*}\end{bmatrix}=\frac{\Delta t}{\xi_1}\begin{bmatrix}M^{-1} & 0\\0 & M^{-1}\end{bmatrix}\begin{bmatrix}D_1^T & 0\\0 & D_2^T\end{bmatrix}\begin{bmatrix}\phi_{,\Delta t}^{n+1}\\\phi_{,\Delta t}^{n+1}\end{bmatrix}$$

By applying continuity, i.e., $[D_1,D_2]\begin{bmatrix}u_1\\u_2\end{bmatrix}=0$ *to the LHS of above we get*

$$-\left(D_1 u_1^* + D_2 u^*\right) = \frac{\Delta t}{\xi_1}\left(D_1 M^{-1} D_1^T + D_2 M^{-1} D_2^T\right)\phi_{,\Delta t}^{n+1}$$

Call

$$E = \left(D_1 M^{-1} D_1^T + D_2 M^{-1} D_2^T\right)$$

$$E\phi_{,\Delta t}^{n+1} = -\frac{\xi_1}{\Delta t}\left(D_1 u_1^* + D_2 u^*\right) \text{ where } E = \left(D_1 M^{-1} D_1^T + D_2 M^{-1} D_2^T\right) \quad (3.35)$$

Solving the above gives the pressure constraint scalar, $\phi_{,\Delta t}^{n+1}$.

See section 3.5.2 for the alternate ways of handling the difficulties involved in dealing with the inverse mass matrix, M^{-1}.

2-Approximate pressure method

The Approximate pressure method directly discretizes the equation (3.21). The corresponding matrix form can be written as

$$K_p \phi_{,\Delta t}^{n+1} = -\frac{\xi_1}{\Delta t}\left(D_1 u_1^* + D_2 u_2^*\right) \quad (3.36)$$

Update of pressure like parameter.

$$q^{n+1} = q^n + \phi_{,\Delta t}^{n+1}$$

Type I

$$q^{*,n+1} = q^{n+1} \text{ and}$$

Type II

$$q^{*,n+2} = 2q^{n+1} - q^n$$

Type IV

$M_p q^{n+1} = M_p\left(q^{*,n+1} + \phi_{,\Delta t}^{n+1}\right) - \nu\left(D_1 u_1^* + D_2 u_2^*\right)$ *where* M_p *pressure-mass matrix derived from elements used for pressure.*

Type III

$$q^{*,n+1} = q^{n+1}$$

Type IV

$$q^{*,n+2} = 2q^{n+1} - q^{n}$$

c) Velocity Projection step

Once ϕ is computed, the velocity field u^* can be projected into a solenoidal field to obtain u. From equation (3.34) we have the matrix form

$$\begin{bmatrix} u_1^{n+1} \\ u_2^{n+1} \end{bmatrix} - \begin{bmatrix} u_1^{*} \\ u_2^{*} \end{bmatrix} = \frac{\Delta t}{\xi_1} \begin{bmatrix} M^{-1} & 0 \\ 0 & M^{-1} \end{bmatrix} \begin{bmatrix} D_1^T & 0 \\ 0 & D_2^T \end{bmatrix} \begin{bmatrix} \phi_{,\Delta t}^{n+1} \\ \phi_{,\Delta t}^{n+1} \end{bmatrix}$$

Note that the above expression does not force to invert the mass matrix as it can be written as a explicit expression of the mass matrix. This fact allows solving the equation to obtain the projected velocity as opposed to computing it via the inverse mass formulation shown above. This is in contrast to E matrix, which has inverse mass matrix implicitly in its definition thus needing the inverse mass matrix.

3.5.2 Variation of Matrix implementations of Classical Methods

There are a few different possibilities when solving the above equation (3.34). We shall consider three methods based on the degree of approximation made to the mass matrix.

1. ***Full Classical Method***

   The pressure constraint parameter is solved using

   $$E = \left(D_1 M^{-1} D_1^T + D_2 M^{-1} D_2^T\right)$$

   Where M^{-1} is the inverse of the full mass matrix. There is no explicit expression with mass, therefore mass matrix need to be inverted. The inverse of the banded mass matrix obtained in TH elements result in a fully dense matrix as the inverse. Due to computational cost involved in inverting and storing the mass matrix and E, this method remains an academic one for Taylor-Hood elements. In spectral method, where orthogonal shape functions are sometimes used, the full classical method remains viable due to mass matrix being a diagonal matrix.

2. ***Lumped Mass Method***

   This method facilitates an easy inversion of the mass matrix by substituting a lumped mass matrix, instead of the full mass matrix. The diagonal nature of the lumped mass matrix affords an easy inversion of it.

   $$E = \left(D_1 M_L^{-1} D_1^T + D_2 M_L^{-1} D_2^T\right) \qquad (3.37)$$

   Where M_L^{-1} is the inverse of the lumped mass matrix.

   The projected velocity is obtained by solving

$$\begin{bmatrix} M_L & 0 \\ 0 & M_L \end{bmatrix} \begin{bmatrix} u_1^{n+1} \\ u_2^{n+1} \end{bmatrix} - \begin{bmatrix} M_L & 0 \\ 0 & M_L \end{bmatrix} \begin{bmatrix} u_1^{*} \\ u_2^{*} \end{bmatrix} = \frac{\Delta t}{\xi_1} \begin{bmatrix} D_1^T & 0 \\ 0 & D_2^T \end{bmatrix} \begin{bmatrix} \phi_{,\Delta t}^{n+1} \\ \phi_{,\Delta t}^{n+1} \end{bmatrix}. \qquad (3.38)$$

The present study found mixing of the lumped and full mass matrices strategically lead to an unstable scheme. Therefore one could not use M_L^{-1} for the computation of E matrix and then proceed to solve (3.38) with the full mass matrix.

3. ***The mixed matrix method (M3).***

Here, a novel way of mixing the full and lump matrices to obtain a stable, robust scheme is developed. The method uses lumped mass matrix to compute the pressure constraint scalar ϕ and the projected velocity field u^{n+1} just the same way as above lump mass method using (3.37) and (3.38). But instead of using ϕ computed to obtain the pressure update parameter q, one uses (3.34)

$$\begin{bmatrix} D_1^T & 0 \\ 0 & D_2^T \end{bmatrix} \begin{bmatrix} \phi_{,\Delta t}^{n+1} \\ \phi_{,\Delta t}^{n+1} \end{bmatrix} = \frac{\xi_1}{\Delta t} \begin{bmatrix} M & 0 \\ 0 & M \end{bmatrix} \begin{bmatrix} u_1^{n+1} - u_1^* \\ u_2^{n+1} - u_2^* \end{bmatrix}$$

to approximate the pressure gradient terms in the momentum equation. In other words, the two velocity fields of u and u^* are used to estimate $\overline{D}\phi$. This, in tern, is used directly to approximate $\overline{D}q$ which is used in the momentum equation. Consequently, q is never explicitly computed and the computed $\phi_{,\Delta t}$ is discarded (only used as the initial guess in the CG solver for the proceeding step). The imposition of the boundary conditions $u\,|_\Gamma = 0$ yields

$$\begin{bmatrix} u_1^{n+1} - u_1^* \\ u_2^{n+1} - u_2^* \end{bmatrix}_{\partial\Omega} = 0.$$

3.6 On Equivalence to the Solving the Global Matrix

When studying the splitting methods, one of the interesting facts to note is the possibility of arriving at identical algorithms to Algebraic techniques on matrices. The existence of these algebraic equivalences shed a light in our understanding of so called *splitting error.* In the literature often the splitting error is attributed to the decoupling of velocity and pressure in the solution process. From the analysis below we could speculate that much of the documented errors, such as the numerical boundary layer, could be attributed to incorrect or incomplete boundary conditions and not in the split itself.

The matrix equations (3.32) and (3.33) representing Navier-Stokes equations yield a global matrix of

$$\begin{bmatrix} \frac{K}{\mathrm{Re}}+\frac{M}{\Delta t} & 0 & D_1^T \\ 0 & \frac{K}{\mathrm{Re}}+\frac{M}{\Delta t} & D_2^T \\ D_1 & D_2 & 0 \end{bmatrix} \begin{bmatrix} u_1^* \\ u_2^* \\ p^{n+1} \end{bmatrix} = \begin{bmatrix} f_1 \\ f_2 \\ 0 \end{bmatrix} \tag{3.39}$$

where f_1 and f_2 are the explicit terms including the advection term.

It is interesting to note that, a method strongly resembling Fractional Splitting Method could be obtained purely by considering inexact LU factorization.

First, the general matrix format of above is,

$$\begin{bmatrix} \frac{\overline{K}}{\mathrm{Re}}+\frac{\overline{M}}{\Delta t} & \overline{D}^T \\ \overline{D} & 0 \end{bmatrix} \begin{bmatrix} U^{n+1} \\ p^{n+1} \end{bmatrix} = \begin{bmatrix} \frac{\overline{M}U^n}{\Delta t}+F^{n+1} \\ 0 \end{bmatrix} \tag{3.40}$$

The inexact LU factorization method is based on the approximation

$$\begin{bmatrix} \frac{\overline{K}}{\mathrm{Re}}+\frac{\overline{M}}{\Delta t} & \overline{D}^T \\ \overline{D} & 0 \end{bmatrix}\begin{bmatrix} U^{n+1} \\ p^{n+1} \end{bmatrix} \approx \begin{bmatrix} \frac{\overline{K}}{\mathrm{Re}}+\frac{\overline{M}}{\Delta t} & 0 \\ \overline{D} & -\Delta t\overline{D}\overline{M}^{-1}\overline{D}^T \end{bmatrix}\begin{bmatrix} \bar{I} & \Delta t\overline{M}^{-1}\overline{D}^T \\ 0 & \bar{I} \end{bmatrix}$$

The four steps of the solution process by inexact LU containing the approximate solution are

$$\left(\frac{\overline{K}}{\mathrm{Re}}+\frac{\overline{M}}{\Delta t}\right)\tilde{U}^{n+1} = \frac{\overline{M}}{\Delta t}U^n + F^{n+1} \tag{3.41}$$

$$\overline{D}\overline{M}^{-1}\overline{D}^{-1}\Phi^{n+1} = \frac{1}{\Delta t}\overline{D}\tilde{U}^{n+1} \tag{3.42}$$

$$U^{n+1} = \tilde{U}^{n+1} - \Delta t\overline{M}^{-1}\overline{D}^T\Phi^{n+1} \tag{3.43}$$

$$p^{n+1} = \Phi^{n+1} \tag{4.44}$$

The incremental pressure scheme could be obtained by breaking down

$$\begin{bmatrix} \frac{\overline{K}}{\mathrm{Re}}+\frac{\overline{M}}{\Delta t} & \overline{D}^T \\ \overline{D} & 0 \end{bmatrix}\begin{bmatrix} U^{n+1} \\ p^{n+1}-p^n \end{bmatrix} = \begin{bmatrix} \frac{\overline{M}U^n}{\Delta t}+F^{n+1}-\overline{D}^T p^n \\ 0 \end{bmatrix}$$

to four steps below

$$\left(\frac{\overline{K}}{\mathrm{Re}}+\frac{\overline{M}}{\Delta t}\right)\tilde{U}^{n+1} = \frac{\overline{M}}{\Delta t}U^n + F^{n+1} - \overline{D}^T p^n \tag{4.45}$$

$$\overline{D}\overline{M}^{-1}\overline{D}^{-1}\Phi^{n+1} = \frac{1}{\Delta t}\overline{D}\tilde{U}^{n+1} \tag{4.46}$$

$$U^{n+1} = \tilde{U}^{n+1} - \Delta t\overline{M}^{-1}\overline{D}^{T}\Phi^{n+1} \tag{4.47}$$

$$p^{n+1} = \Phi^{n+1} + p^{n} \tag{4.48}$$

Note that the above equations do not explicitly employ any artificial boundary conditions. Dirichlet boundary conditions could be imposed on (3.39) matrix equation. The above equations (3.41) to (3.44) represent the Chorin's original splitting method (see section 3.2.1) with Classical pressure computations and the equations (4.45) to (4.48) the Chorin-Temam (see section 3.3.1) method (albeit without the rotational pressure update term proposed by Guermond). The present study finds that the numerical boundary layer in pressure solution is observed when equation (3.39) is, in its entirety, solved via a direct solver as well as well as when solved using Chorin-Temam method. The matrix equivalence of the direct solution to (3.39) to Chorin-Temam method strongly suggest that the source of the numerical boundary layer is not the split itself but a more general inadequacy in specification of the boundary conditions to the Navier-Stokes equations.

4. Consistent Splitting Methods

The Consistent Splitting methods differ from Fractional Splitting methods in one significant aspect where the former does not project the velocity field, computed via solving the momentum equation, to a solenoidal vector field. The continuity is achieved via the boundary conditions on the constraint scalar in case of the Gauge methods and via the rotational term in Guermond's Consistent Pressure method. Both methods are reported to have second order convergence in pressure. These methods are often implemented in higher order methods such as Spectral methods. Gauge method has been implemented in Finite Difference Method [7].

4.1 The Gauge Method

The Gauge field method introduced by E and Liu [14] demonstrates that a second order convergence of pressure could be attained via the gauge term that corrects the pressure (or the gradient of the pressure) by taking into consideration both normal and tangent boundary conditions. E and Liu were first to identify the gauge term, ϕ. Previous methods that are studied in present work considered ϕ as being either the pressure at time step n, p^n or as a pressure correction term dp^n. The relationship between the gauge term and the correct pressure, equation (3.7) or (3.8) was obtained by the authors. E and Liu [14] recognized that the gauge variable affords more general boundary conditions than the pressure. They considered the Gauge method to be classified as a consistent method not as a Fractional Splitting method of solving Navier-Stokes equations. Guremond, Minev and Shen [22] showed that the Gauge method is mathematically equivalent to the Consistent Pressure Method (CPM) proposed by themselves which is described in section 4.2. The intermediate velocity computed u^* is called an *auxiliary* vector field a. There are two possible sets of unambiguous boundary conditions.

$$\left.\frac{\partial\phi}{\partial n}\right|_{\partial\Omega}=0 \qquad a\cdot n|_{\partial\Omega}=0 \qquad a\cdot\tau|_{\partial\Omega}=\left.\frac{\partial\phi}{\partial\tau}\right|_{\partial\Omega} \tag{4.1}$$

or

$$\phi|_{\partial\Omega}=0 \qquad u^{*}\cdot n|_{\partial\Omega}=\left.\frac{\partial\phi}{\partial n}\right|_{\partial\Omega} \qquad u^{*}\cdot\tau|_{\partial\Omega}=0 \tag{4.2}$$

where τ is the unit tangent vector at the boundary.

The general algorithm for the first set of boundary values is given below.

(a) solving the momentum equation for a^{n+1}

$$\frac{\xi_1 a^{n+1}-\xi_2 a^{n}+\xi_3 a^{n-1}}{\Delta t}-\nabla\nu\nabla a^{n+1}+\left(u\cdot\nabla u\right)^{*,n+1}=f^{n+1} \tag{4.3}$$

with boundary conditions

$$a^{n+1}\cdot n\,|_{\Gamma=0}=0, \qquad a^{n+1}\cdot\tau\,|_{\Gamma=0}=-2\frac{\partial\phi^{n}}{\partial\tau}+\frac{\partial\phi^{n-1}}{\partial\tau} \tag{4.4}$$

(b) pressure constraint scalar

$$\nabla^{2}\phi^{n+1}=\nabla\cdot a^{n+1}$$

with natural boundary condition

$$\left.\frac{\partial\phi^{n+1}}{\partial n}\right|_{\Gamma=0}=0$$

(c) velocity update

$$u^{n+1} = a^{n+1} - \nabla \phi^{n+1} \tag{4.5}$$

Similarly, the second set of boundary conditions also yields a consistent Gauge method as well. We have derived the above algorithm as it is used in the proof of equivalence to the Consistent Pressure method introduced in the next section by Guermons, Minev and Shen[22].

4.2 Guermond's Consistent Pressure Method

Numerous works that either solve the pressure convergence problem or circumvent it has been published. Guermond and Shen [24] proposed a "truly consistent " splitting scheme. This scheme is based on pressure Poisson equation (approximate pressure) but the velocity is not projected to a solenoidal field. Similar to traditional splitting methods, for each time step, a Helmholtz type equation is solved but the right hand side of the equation is formulated such that it carries the rotational information of the flow. A corrective term, via the divergence of the computed velocity, is introduced to the pressure update (Type IV). The authors demonstrate the second order convergence of pressure on a Dirichlet no-slip flow and graphically demonstrate the reduction of the numerical boundary layer. An artificial flow solution that employed a forcing function on NS equation is employed in the study.

In deriving the technique, the key idea that Guermond et.al. use is to test the momentum equation against the gradients.

Take L^2 inner product of the momentum equation with respect to $\nabla\phi$

$$\int_{\Omega}\nabla q\cdot\nabla\varphi dx=\int_{\Omega}(f-u\cdot\nabla u+\nabla\nu\nabla u)\cdot\nabla\varphi dx \tag{4.6}$$

Note $(u_t,\nabla\varphi)=-(\nabla\cdot u_t,\varphi)=0$ (4.7)

The momentum equation is given by

$$\left(\frac{Du^*}{\Delta t},\nabla\varphi\right)+B(u^n\cdot\nabla u^n,\nabla\varphi)+(\nabla q^{*,n+1},\nabla\varphi)=(\nu\nabla^2u^*,\nabla\varphi)\quad u\mid_{\partial\Omega}=u_b \tag{4.8}$$

By imposing $(u_t,\nabla\varphi)=-(\nabla\cdot u_t,\varphi)=0$ and by the identity

$$\nabla^2 u = \nabla\nabla\cdot u - \nabla\times\nabla\times u \tag{4.9}$$

note $\nabla\times\nabla\times u = \nabla\times\nabla\times u^*$.

$$\left(u^n\cdot\nabla u^n,\nabla\varphi\right)+\left(\nabla q^{n+1},\nabla\varphi\right)=\left(-\nu\nabla\times\nabla\times\nabla u^{n+1},\nabla\varphi\right) \tag{4.10}$$

Subtracting the above two (4.8) from (4.10) gives

$$-\left(\frac{Du^*}{\Delta t},\nabla\varphi\right)+\left(\nabla\left(q^{n+1}-q^{*,n+1}\right),\nabla\varphi\right)=-\left(\nu\nabla\nabla\cdot u^{n+1},\nabla\varphi\right)$$

Re writing the above with pressure constraint parameter ϕ

$$\left(\nabla\phi^{n+1}_{,\Delta t},\nabla\varphi\right)=\left(\frac{Du^*}{\Delta t},\nabla\varphi\right) \tag{4.11}$$

Where

$$\phi^{n+1}_{,\Delta t} = q^{n+1} - q^* + \nu\nabla\cdot u^*. \tag{4.12}$$

Re arranging, we obtain naturally, an update formula for the pressure like parameter.

$$q^{n+1} = q^* + \phi^{n+1}_{,\Delta t} - \nu\nabla\cdot u^*$$

And final update that Guermond proposes is

$$q^* = 2q^{n+1} - q^n$$

Note that continuity, $\nabla \cdot u = 0$, is assumed *a priori* in the derivations and not imposed during the solution process as in projection methods. The linchpin of this method is the fact that this kind of an indirect imposition of divergence free condition on vector field actually lead to accurate solutions in continuity, pressure and vorticity.

We have called the solution of the momentum equation u^* to keep in common with our mathematical symbolism. Since Consistent Splitting methods do not project the velocity field onto a solenoidal field, the superscript * indicates the newly computed velocity field and u^i where $i \leq n$ are velocity solution fields of previous time steps.

4.2.1 Weak Form Description of Consistent Pressure Method (CPM)

The above developments could now be summarised in the general algorithm description below.

(a) Adjective/Diffusive prediction: $u^n \rightarrow u^*$

$$\left(\frac{Du^*}{\Delta t}, v\right) + B(u^n; u^n, v) - (q^n, \nabla \cdot v) = a(u^*, v) \qquad u\,|_{\partial\Omega} = u_b \qquad \forall v \in X \tag{4.13}$$

(b) Pressure Constraint Scalar:

$$(\nabla \phi^{n+1}_{,\Delta t}, \nabla \varphi) = \frac{1}{\Delta t}(Du^*, \varphi) \qquad\qquad u^*\,|_{\partial\Omega} = u_b \quad \forall \varphi \in M \tag{4.14}$$

(c) Type IV pressure update

$$(q^{n+1}, \varphi) = (q^* + \phi^{n+1}_{,\Delta t} - \nu \nabla \cdot u^*, \varphi)$$

Note: no velocity projection is done.

And

$$q^* = 2q^{n+1} - q^n$$

4.2.2 Matrix Form of Consistent Pressure Method

The weak form momentum equation, presented by equation (4.13), could be written in matrix form as

$$\begin{bmatrix} K + \frac{\xi_1}{\Delta t} M & 0 \\ 0 & K + \frac{\xi_1}{\Delta t} M \end{bmatrix} \begin{bmatrix} u_1^* \\ u_2^* \end{bmatrix} = -\begin{bmatrix} \frac{M}{\Delta t}\left(\xi_1 u_1^{n-1} + \xi_1 u_1^{n-2}\right) & 0 \\ 0 & \frac{M}{\Delta t}\left(\xi_1 u_2^{n-1} + \xi_1 u_2^{n-2}\right) \end{bmatrix} + \begin{bmatrix} D_1^T & 0 \\ 0 & D_2^T \end{bmatrix} \begin{bmatrix} q^* \\ q^* \end{bmatrix}$$
$$+ \begin{bmatrix} \beta_1 C\left(\bar{u}^n\right) u_1^n + \beta_2 C\left(\bar{u}^{n-1}\right) u_1^{n-1} + \beta_3 C\left(\bar{u}^{n-2}\right) u_1^{n-2} & 0 \\ 0 & \beta_1 C\left(\bar{u}^n\right) u_2^n + \beta_1 C\left(\bar{u}^{n-1}\right) u_2^{n-1} + \beta_1 C\left(\bar{u}^{n-2}\right) u_2^{n-2} \end{bmatrix} +$$
$$+ \begin{bmatrix} M & 0 \\ 0 & M \end{bmatrix} \begin{bmatrix} f_1^{n+1} \\ f_2^{n+1} \end{bmatrix}$$

With boundary conditions

$$u\big|_{\Gamma_{wall}} = 0$$

The the matrix equivalent of equation (4.14), the pressure Laplace equation, could be solved to obtain the pressure constraint scalar by solving

$$K_p \phi_{,\Delta t} = -\frac{1}{\Delta t}\left(D_1^T\left(\xi_1 u_1^* + \xi_2 u_1^{n-1} + \xi_3 u_1^{n-2}\right) + D_2^T\left(\xi_1 u_2^* + \xi^{n-1} u_2^{n-1} + \xi_3 u_2^{n-2}\right)\right) \qquad (4.15)$$

The new pressure update formula could be found by first, solving for q^{n+1}

$$M_p q^{n+1} = M_p\left(q^* + \phi_{,\Delta t}^{n+1}\right) - \left(D_1 u_1^* + D_2 u_2^*\right) \tag{4.16}$$

and then the pressure parameter is updated by

$$q^* = 2q^{n+1} - q^n$$

5 The Splitting Methods Classified

Based on the theoretical considerations presented in the previous chapters, we shall present the final classification of the Splitting methods and select the candidates for the numerical studies. The well-known Kim and Moin method and Gauge method are omitted in the numerical studies in favour of newer Chorin-Temam method with rotational pressure update and Guremond's Consistent Pressure methods respectively. This choice is based on the recent publication of the mathematical equivalence of the older methods to the newer methods. However it is noted that proof of mathematical equivalence many not be the same as similar behaviour due to numerical and computer implementation differences. The methods selected for the numerical studies are:

1. Classical method with full E
2. Classical method with lump mass E
3. Classical mixed mass method (M3)
4. Approximate pressure, Kp, with rotational (type III) pressure update.
5. Guremond's Consistent Pressure method

Of the above methods, the first four falls under Fractional Splitting Method and the last method, the Consistent Pressure Method, falls under the Consistent Splitting Method. Once the equivalences are taken into consideration, the splitting methods that we have considered can be classified as below.

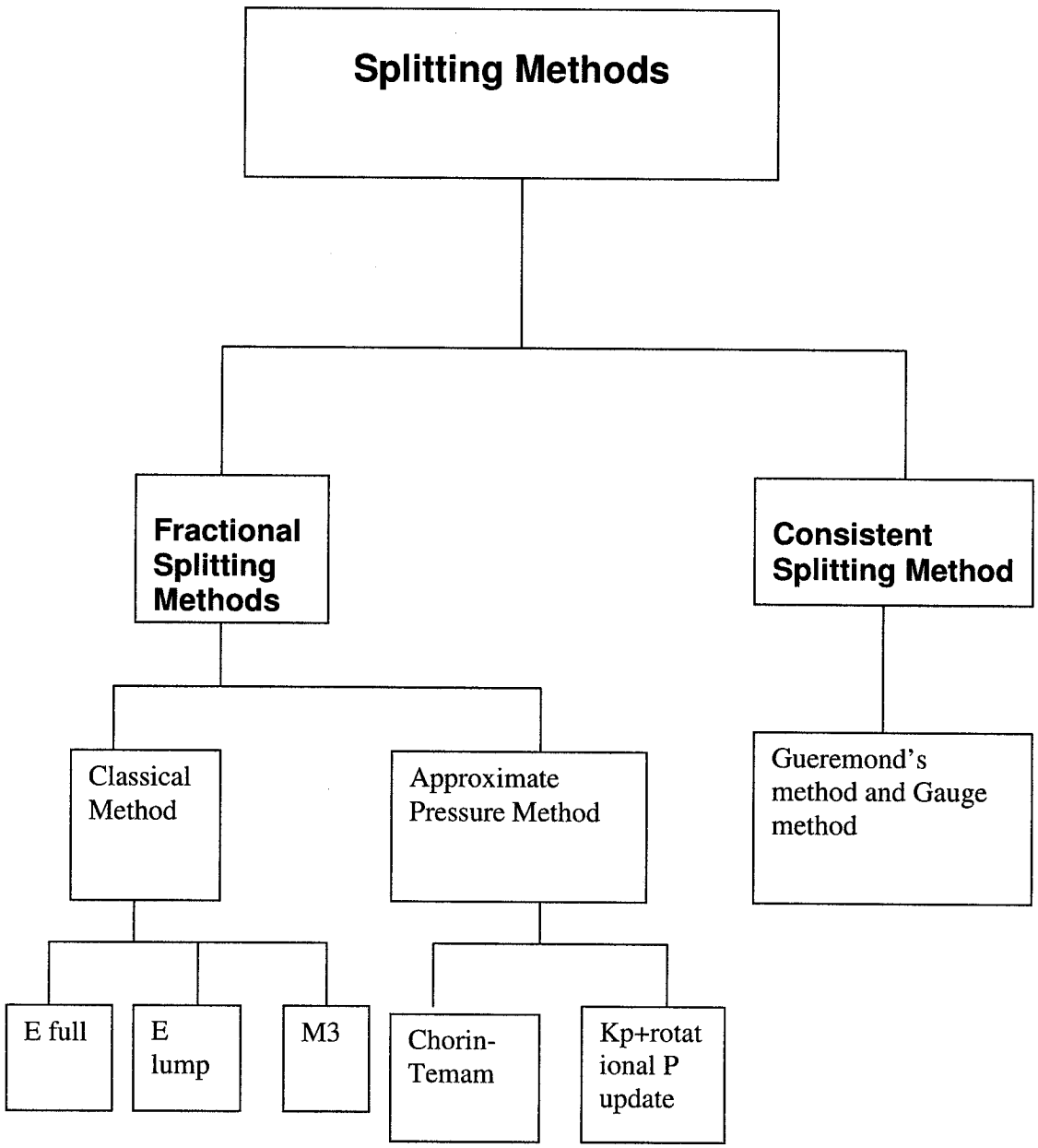

Figure 05
A chart of Splitting Methods that are considered in this study after the equivalences are taken into account.

6. Numerical Simulations

The numerical study is conducted on the schemes selected in Chapter 5 with the emphasis on revealing effects of Type III spatial error introduced in cheaper 1. The three flow fields selected for the study are the Taylor-Green flow, a forced vortical flow with Dirichlet wall boundary condition and the Lid driven Cavity flow. The flows above are selected to isolate and reveal the effects of main phenomena observed such as numerical boundary layer and errors due to vortices. Taylor-Green vortex flow consists of decaying vortices and does not contain any walls in its fully periodic domain. This flow isolates the effects of vorticity from other effects since there are no boundary errors or errors related to grid Reynolds number. In fact the solution is found to be stable at Reynolds number of tens of millions when simulated with 12 x 12 mesh on a $]-\pi,\pi[^2$ domain. The second flow induced by a bulk forcing term to NS equations in a square wall bounded domain. While the solution to this flow is independent of the Reynolds number, the forcing terms are not. This flow is used to highlight the effects related to the numerical boundary layer on pressure. The lid driven cavity flow is a more general flow with vortical region as well as regions of high shear and boundary layers.

The time evolution of the normalized errors of velocity and pressure is presented in their natural norm. The normalized errors are obtained by:

The errors in H_1 norm in velocity is normalized by

$$error(H) = \left[\frac{(u-u_{exact})^T K (u-u_{exact})}{u_{exact}^T K u_{exact}} \right]^{\frac{1}{2}} \tag{5.1}$$

Similarly, the L_2 norm for the pressure is normalized by

$$error(L_2) = \left[\frac{(q - p_{exact})^T M_P (q - p_{exact})}{p_{exact}^T M_P p_{exact}} \right]^{\frac{1}{2}} \tag{5.2}$$

The error in continuity equation is computed by

$$error = \max \left| D_1 u + D_2 v \right| \tag{5.3}$$

The spatial distribution of the continuity is computed by ploting

$$error = D_1 u + D_2 v \tag{5.4}$$

The spatial pressure error distribution is computed by

$$error(L_\infty) = (q - p_{exact}) \tag{5.5}$$

The simulations are made with time steps substantially lower than maximum stable time step ensuring that the errors observed are not due to the stability issues of the time integration scheme. The iterative solver used to solve both the velocity and pressure is the Conjugate Gradient (CG) solver preconditioned with the diagonal of the matrix solved. The extrapolated value of , $2x^n - x^{n-1}$, is used as the initial value of the solution.

The present study finds that the second order pressure update methods (Type II and IV) lead to oscillating errors in pressure (Appendix A). This also reduced the robustness of the solvers some flows. The numerical investigation that follows use type I for classical pressure update methods and type III for the K_P +rotational method.

6.1 Taylor-Green Flow

Taylor-Green flow is an exact solution to Navier-Stokes equations. The domain of the flow is a Tours and in 2D, $T^2 = S^1 \times S^1$. The domain considered is $]-\pi,\pi[^2$, square domain. The numerical domain is constructed by making the square domain and by making opposites edges periodic and the corners identical in the element connectivity.

The Taylor-Hood vortices are simulated by using the following initial solution

$$u(x, y, t) = -\cos(x)\sin(y)\exp\left(-\frac{2t}{\mathrm{Re}}\right)$$

$$v(x, y, t) = \sin(x)\cos(y)\exp\left(-\frac{2t}{\mathrm{Re}}\right)$$

$$p(x, y, t) = -\frac{1}{4}(\cos(2x)+\cos(2y))\exp\left(-\frac{4t}{\mathrm{Re}}\right)$$

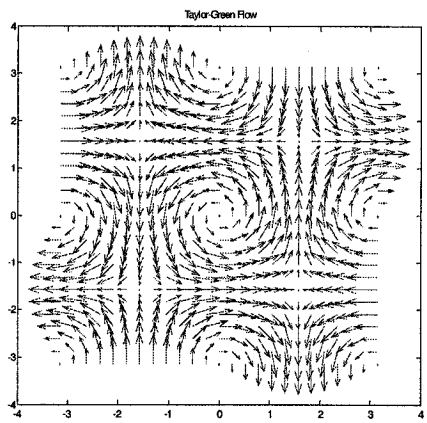

Figure 06
The velocity vector field of Taylor-Green flow.

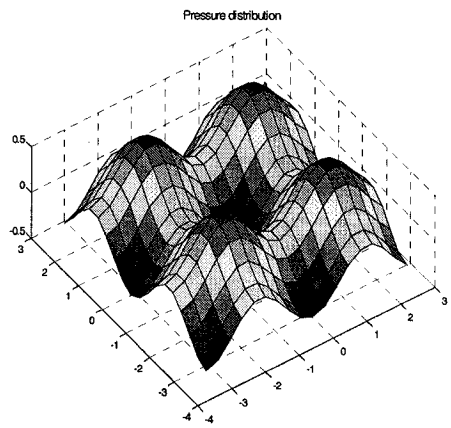

Figure 07
The pressure contour field of the Taylor-Green flow

The Taylor-Green flow is self-similar and decays with time. Figures 06 and 07 graphically represent the solution.

Note that this particular exact solution to the Navier-Stokes equations has an advantage of not requiring a forcing function to be inserted into the solver thus eliminating the possibility of tampering of the solution during the simulation. The *built in* orthogonality $(\nabla\times\nabla\times u,\nabla q)=0$ of the Taylor-Green flow, and the absence of wall boundary conditions, makes it very special, particularly the former from the point of view of splitting methods, thus may not capture all issues of the solution algorithms.

6.1.1 Time Evolution of Taylor-Green Vortex Flow

The time evolution of the Taylor-Green flow is investigated by investigation the errors defined by equations (5.1) to (5.5) for Reynolds numbers 5, 100 and 1000. The time step size is selected to be well inside the CFL/ stability criteria.

Velocity Errors

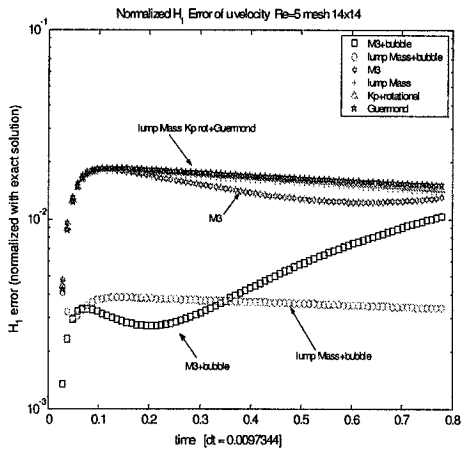

Figure 08
Re=5. Energy norm of normalized u error vs. time

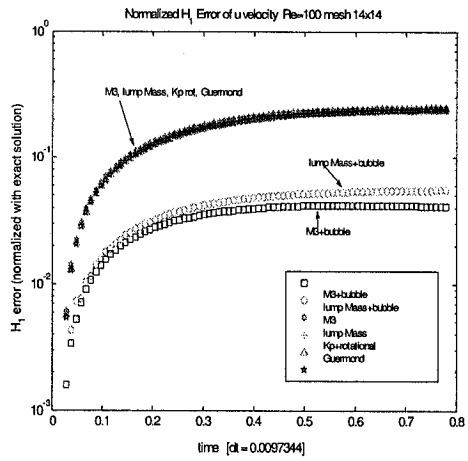

Figure 09
Re=100. Energy norm of normalized u error vs time

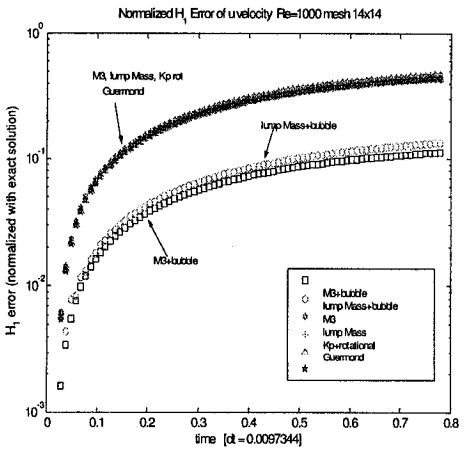

Figure 10
Re=1000. Energy norm of normalized u error vs. time.

From figures 08 to 10, it is observed that the error in velocity increased with increasing Reynolds number. For the Taylor-Green vortex flow, the methods with bubble elements show lower errors.

Pressure errors

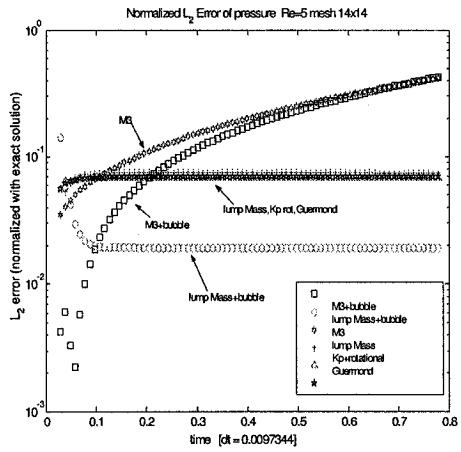

Figure 11
Re=5. The normalized L_2 error of pressure vs. time.

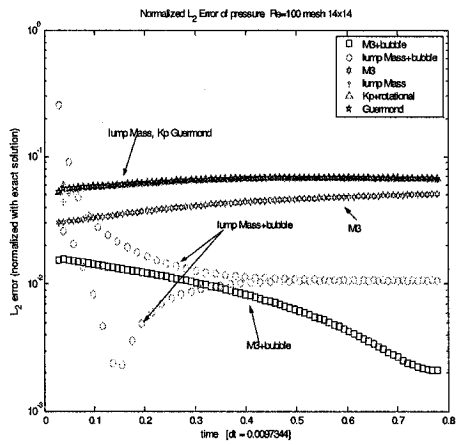

Figure 12
Re=100. The normalized L_2 error of pressure vs time.

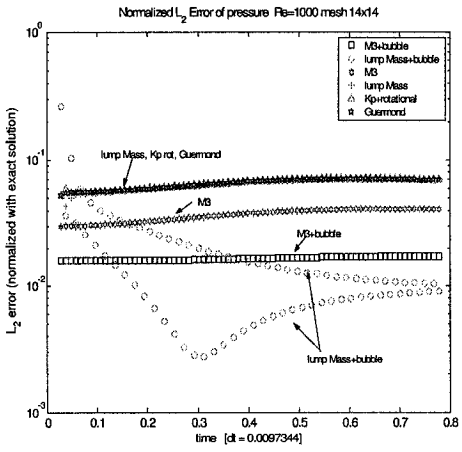

Figure 13
Re=1000. The normalized L_2 error of pressure vs. time.

The figures 11 to 13 indicate that the bubble elements increased the accuracy of the pressure field just as in the case of velocity. M3 method performed better in higher Reynolds numbers while K_P with rotational pressure update and Guermond's CPM method along with lump mass (no bubble) performed better in lower Reynolds numbers. The oscillations observed in lump mass method (figures 12 and 13) with TH+Pbubble is removed by adjusting the weight of the bubble nodes, β, close to unity.

Continuity

The Finite Element Method satisfies the continuity on a global basis. Therefore the global sum of the error in equation (5.4) is a very small number, in the order of the machine epsilon. While present study verifies that this is to be so, a difference in the spatial distribution error is observed for different schemes. For the time evolution of the error of the continuity we shall pick the biggest variation from zero by computing the maximum error by equation (5.3). The spatial distribution of the error is considered in the next section.

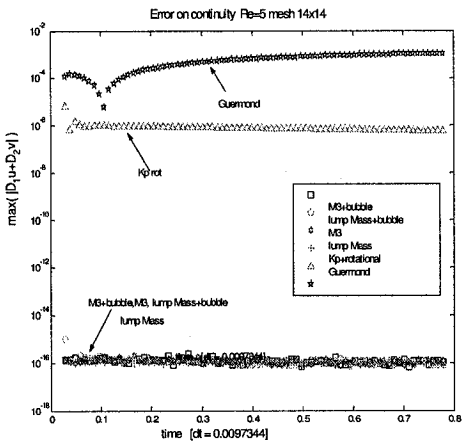

Figure 14
Re=5. The maximum error in continuity vs. time.

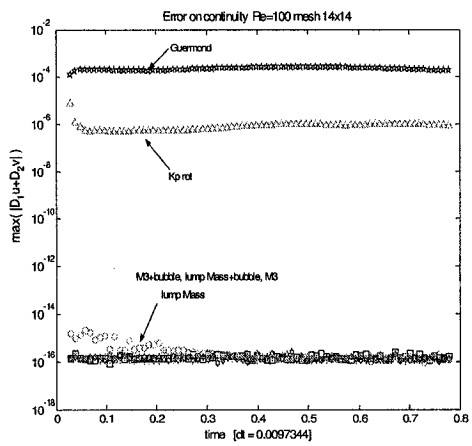

Figure 15
Re=100. The maximum error in continuity vs. time.

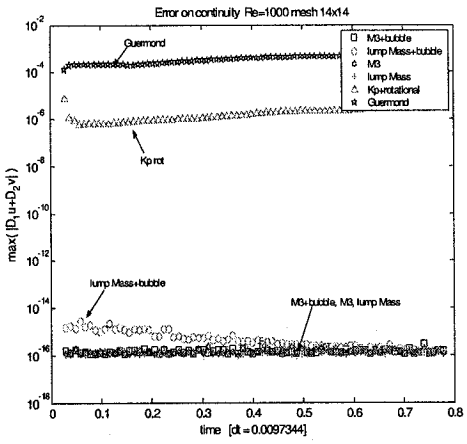

Figure 16
Re=1000. The maximum error on continuity vs. time.

Note from the figures 14 to 16 that the methods that used classical pressure computation methods yield the smallest maximum error on imposing the continuity constraint. Guermond's CPM does not project the velocity onto a solenoidal field and therefore not surprisingly, has the largest error in the continuity. The K_P method is observed o have the second largest error on continuity for Taylor-Green flow.

6.1.2 The Spatial Error Distribution

The spatial error distribution is computed for t=0.5. The values obtained by equation (5.4) for the spatial error distribution for continuity and equation (5.5) for pressure is presented for Reynolds numbers 1, 10 and 100 below.

Re=1

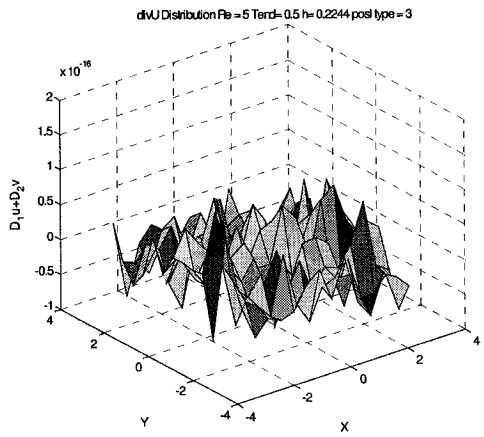

Figure 17
Re=1. M3+bubble continuity spatial error.

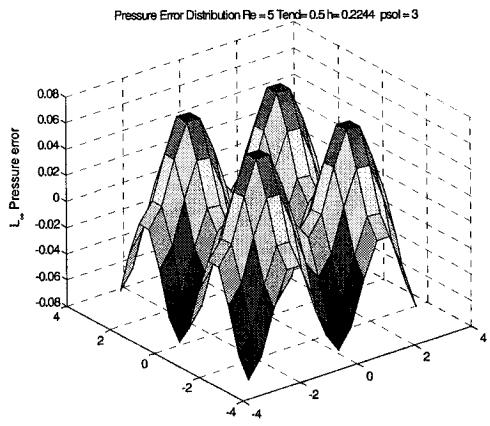

Figure 18
Re=1. M3+bubble pressure spatial error.

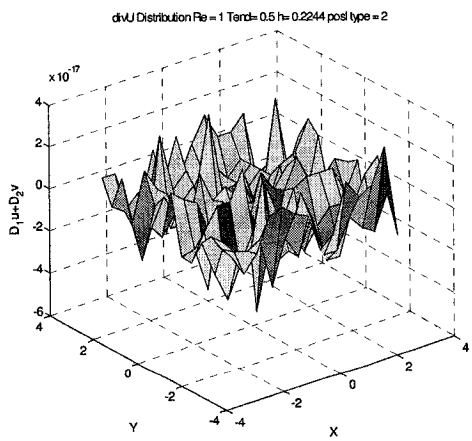

Figure 19
Re=1. lump Mass+bubble continuity spatial error.

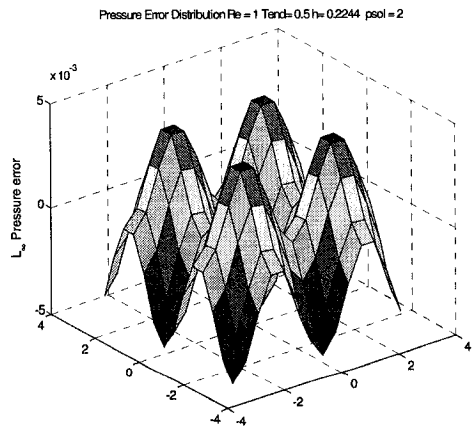

Figure 20
Re=1. lump Mass+bubble pressure spatial error.

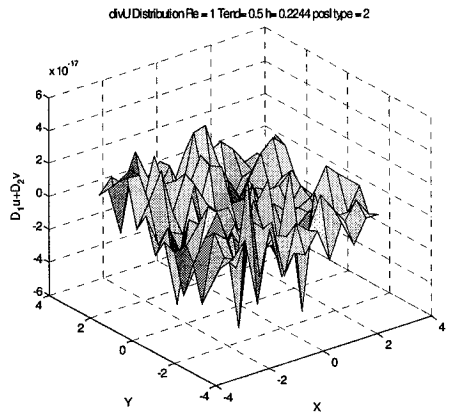

Figure 21
Re=1. lump Mass (no bubble) continuity error.

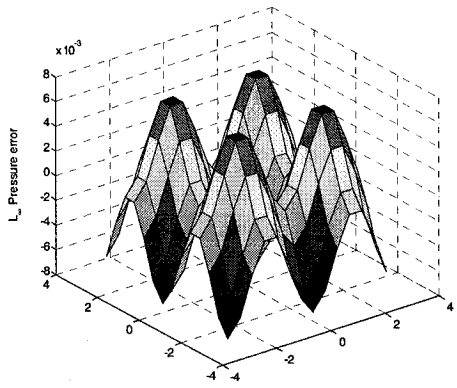

Figure 22
Re=1. lump Mass (no bubble) pressure error

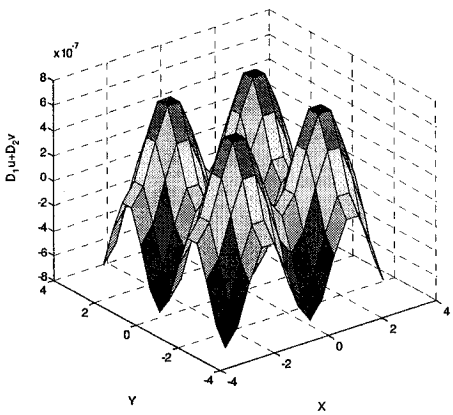

Figure 23
Re=1. K_P+rot P continuity spatial error.

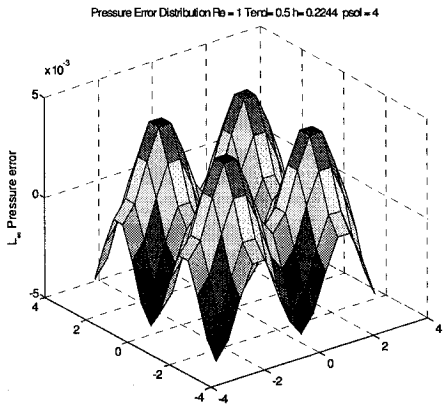

Figure 24
Re=1. K_P +rot P pressure spatial error.

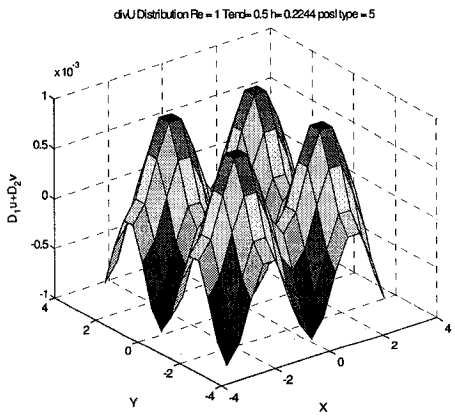

Figure 25
Re=1. Guermond, continuity spatial error.

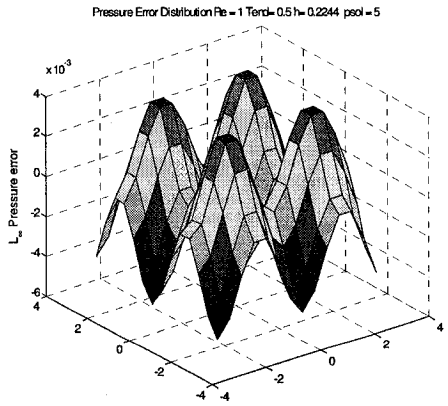

Figure 26
Re=1. Guermond, pressure spatial error.

Re=10

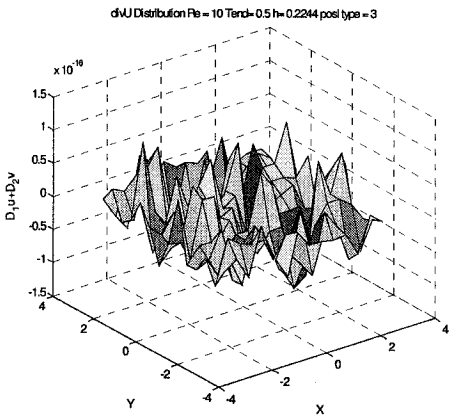

Figure 27
Re=10. M3+bubble continuity spatial error.

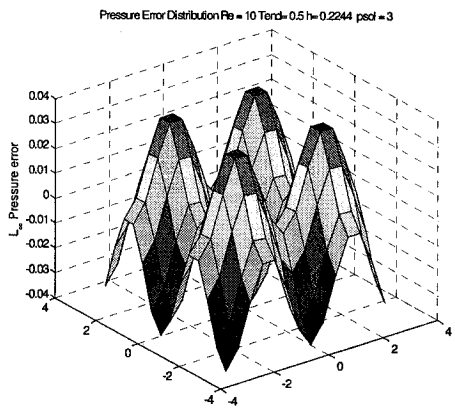

Figure 28
Re=10, M3+bubble pressure spatial error.

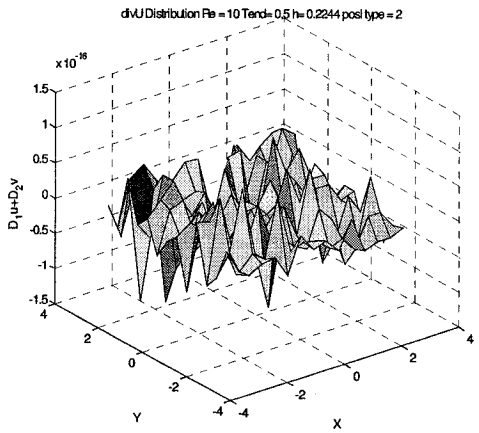

Figure 29
Re=10, lump Mass+bubble continuity spatial error.

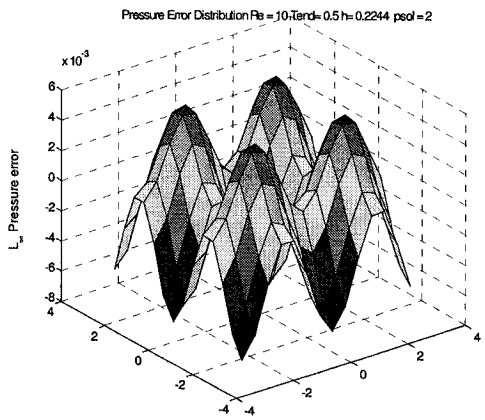

Figure 30
Re=10, lump Mass+bubble pressure error.

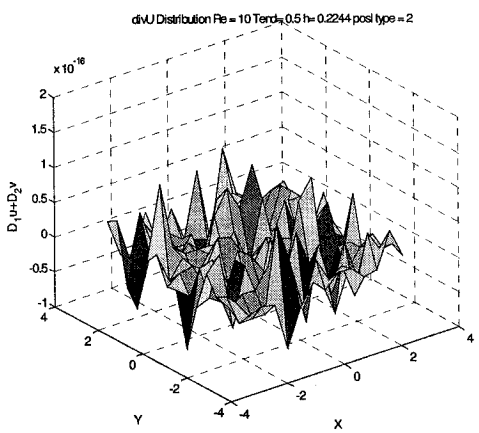

Figure 31
Re=10. lump Mass (no bubble) continuity error.

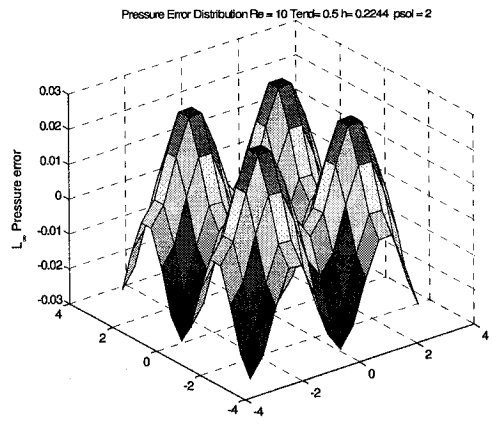

Figure 32
Re=10. lump Mass (no bubble) pressure error.

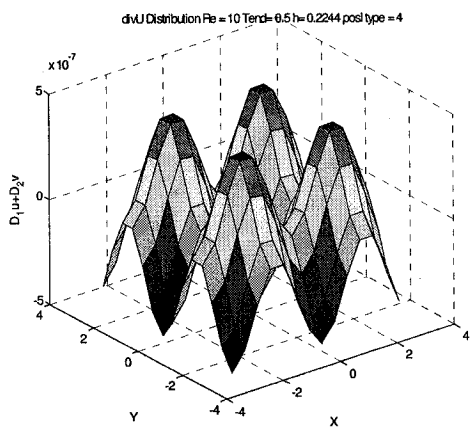

Figure 33
Re=10. K_P +rot continuity spatial error.

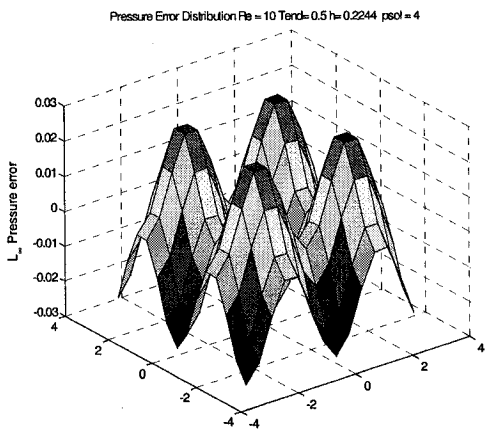

Figure 34
Re=10. K_P +rot pressure spatial error.

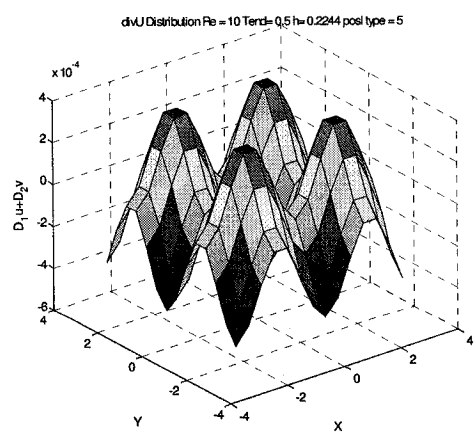

Figure 35
Re=10. Guermond continuity spatial error.

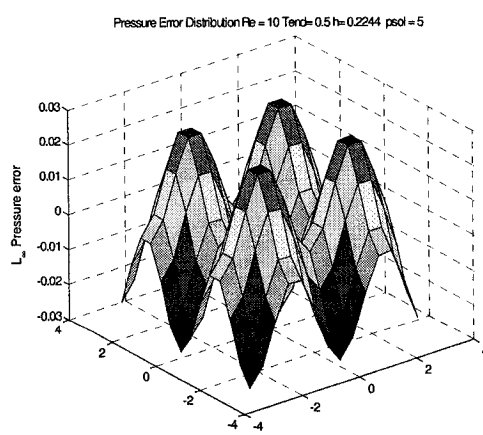

Figure 36
Re=10. Guermond pressure spatial error.

Re=100

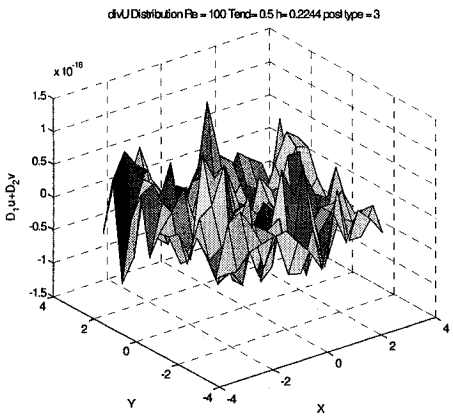

Figure 37
Re=100. M3+bubble continuity spatial error.

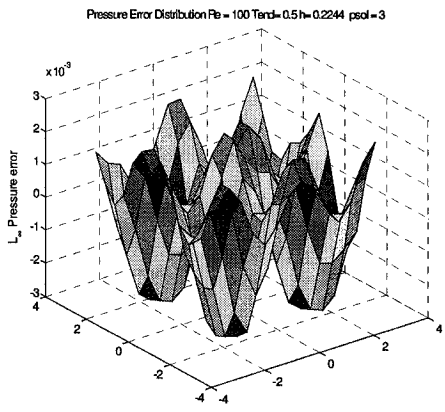

Figure 38
Re=100. M3+bubble pressure spatial error.

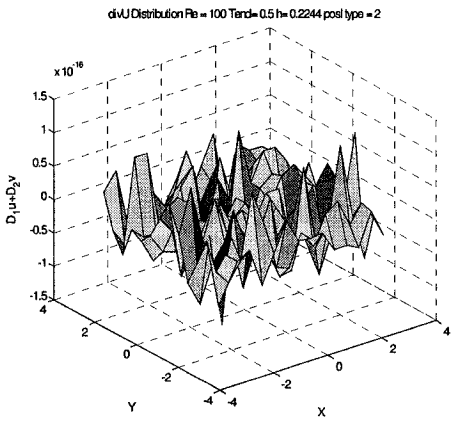

Figure 39
Re=100. lump Mass+bubble continuity error.

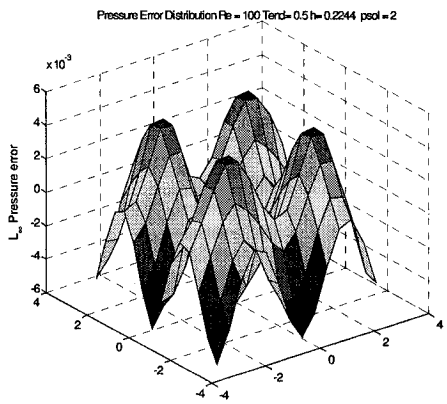

Figure 40
Re=100. lump Mass+bubble pressure error

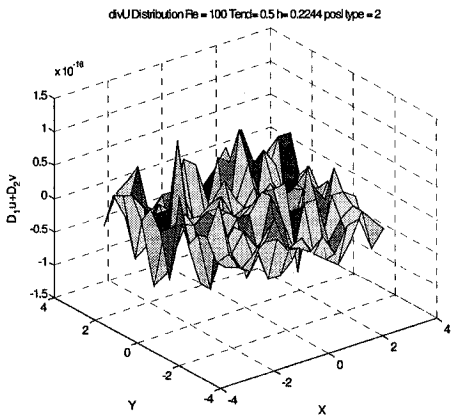

Figure 41
Re=100. lump mass (no bubble) continuity error.

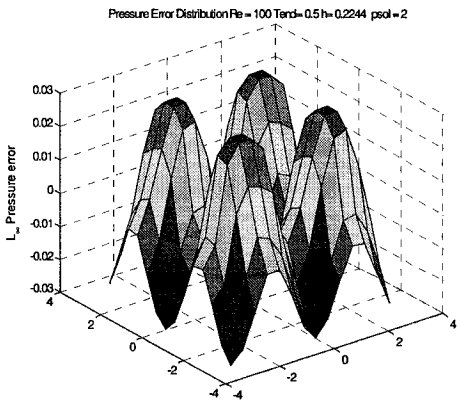

Figure 42
Re=100. lump mass (no bubble) pressure error.

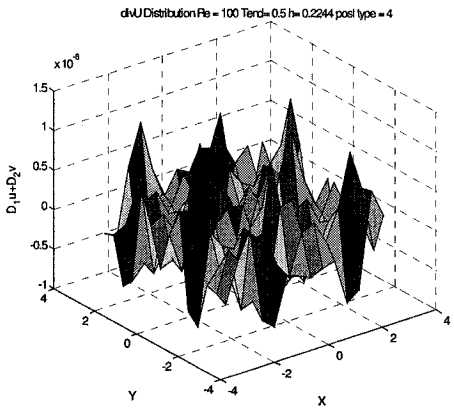

Figure 43
Re=100. K_P continuity spatial error.

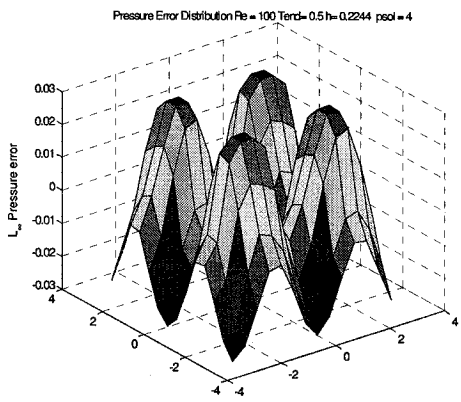

Figure 44
Re=100. K_P pressure spatial error

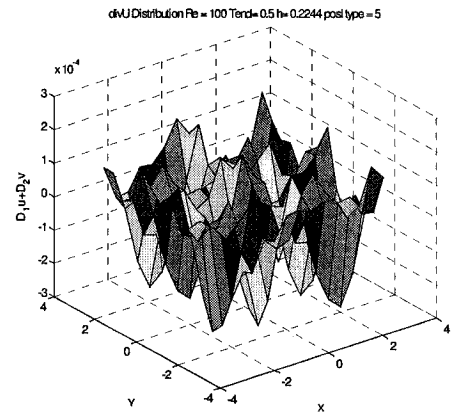

Figure 45
Re=100. Guermond continuity spatial error.

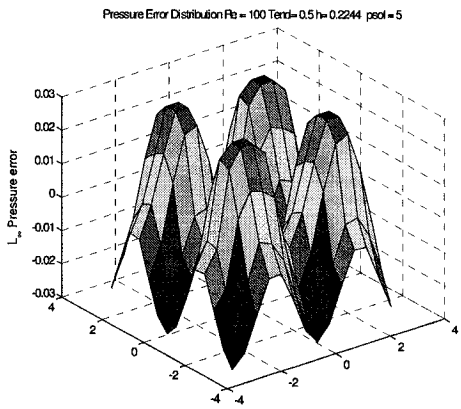

Figure 46
Re=100. Guermond, pressure spatial error.

For the range of the Reynolds numbers considered, the vortex flow results in the largest errors in pressure at centres of the vortex and at the corners of the vortices with signs of error positive and negative respectively (figures 22, 24, 26, 28, 30, 28, 34, 36, 38, 40, 42, 44, 46). At Re=100, M3 method with bubbles has pressure errors sign reversed (figure 38). The M3 method without bubbles and all the other methods considered however, do not experience a sign reversal. The continuity error fields of all methods that use classical method to update pressure (figures 17, 19, 21, 27, 29, 31, 37, 39, 41) reveal that the error in continuity is substantially lower than that of approximate pressure methods

(figures 23, 25, 33, 35, 43, 45). For the approximate pressure methods, the errors in pressures (figures 24, 26, 34, 36, 44, 46) are reflected in the errors in continuity (figures 23, 25, 33, 35, 44, 45) and are much higher.

6.2 Forced Flow with Wall Domain

The Taylor-Green flow in the previous section is studied on a fully periodic domain that is topologically a torus. The effects of the wall boundary conditions are investigated on square domain $]0,1[^2$. The exact solution of

$$U(x,y,t)=\pi\sin(t)\left(\sin(2\pi y)\sin^2(\pi x),-\sin(2\pi x)\sin^2(\pi y)\right) \tag{5.6}$$

$$p(x,y,t)=\sin(t)\cos(\pi x)\sin(\pi y) \tag{5.7}$$

is imposed via a bulk forcing function

$$F=U_t+U\cdot\nabla U-\nu\nabla^2U+\nabla p \tag{5.8}$$

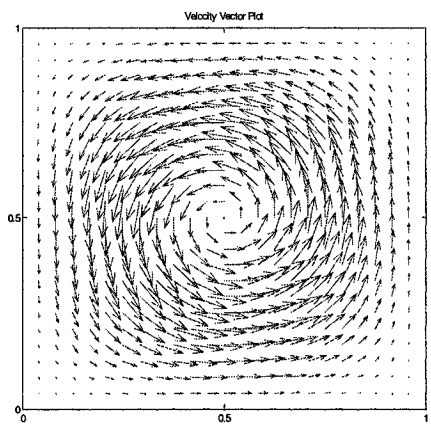

Figure 47
Vector plot of field described by equation (5.6).

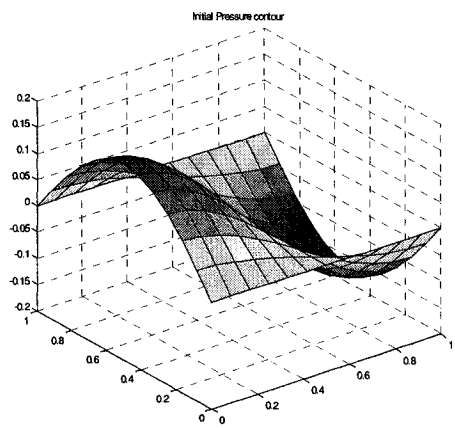

Figure 48
Pressure contour plot of equation (5.7).

Note that velocity and pressure shown in figure 47 and 48 are scaled by sin of time and thus becomes zero periodically. Furthermore, the solutions do not contain the Reynolds number.

6.2.1 Time Evolution of the solution

The time evolution of the Forced flow of type described by equations (5.6) to (5.8) is investigated by investigation the errors defined by equations (5.1) to (5.5) for Reynolds numbers 1, 10 and 100. The time step size is selected to be well inside the CFL/stability criteria.

Velocity Errors

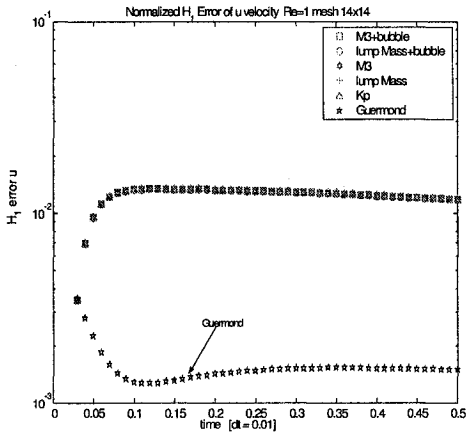

Figure 49
Re=1. Time evolution of the velocity error.

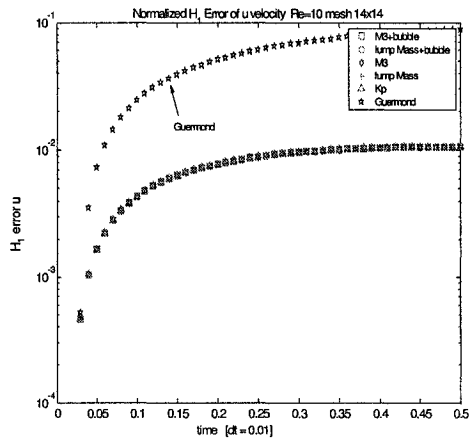

Figure 50
Re=10. Time evolution of the velocity error.

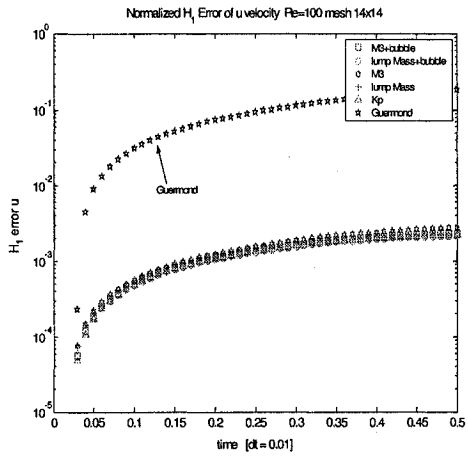

Figure 51
Re=100. Time evolution of the velocity error.

Pressure Errors

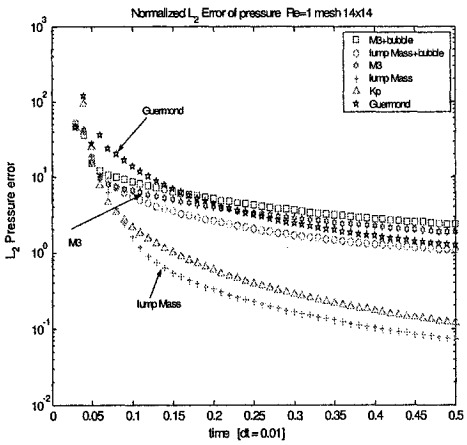

Figure 52
Re=1. Time evolution of pressure error.

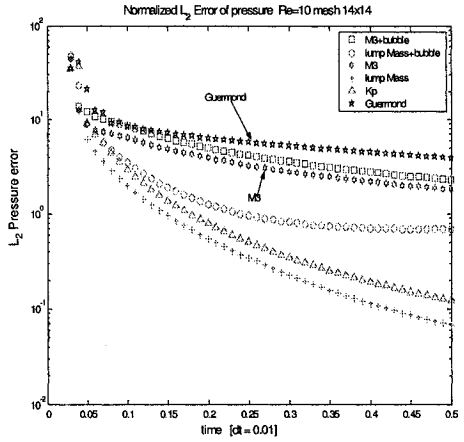

Figure 53
Re=10. Time evolution of pressure error.

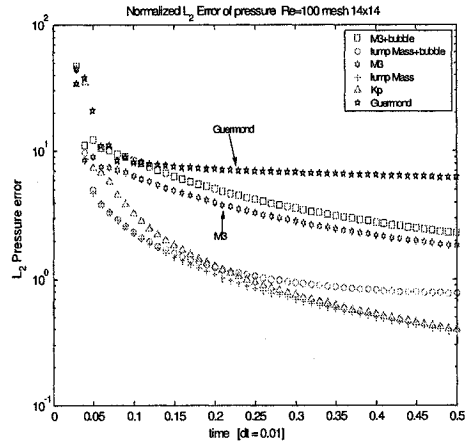

Figure 54
Re=100. Time evolution of the pressure error.

Error in Continuity

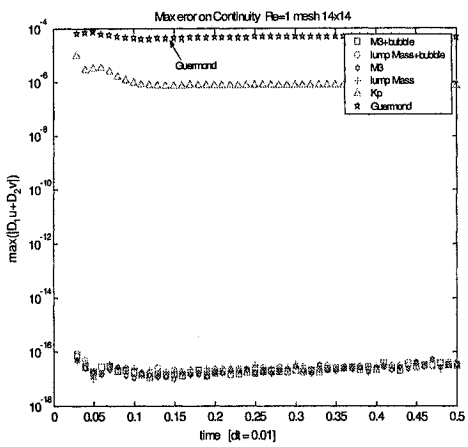

Figure 55
Re=1. Time evolution of continuity error.

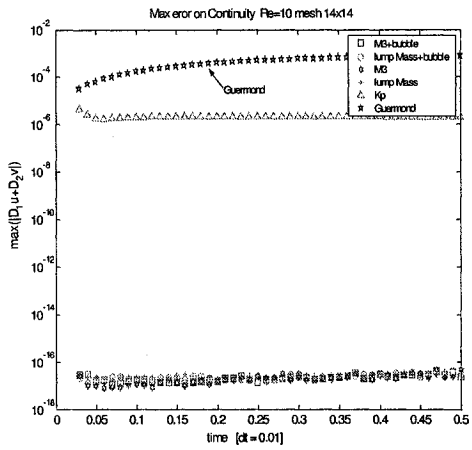

Figure 56
Re=10. Time evolution of the continuity error.

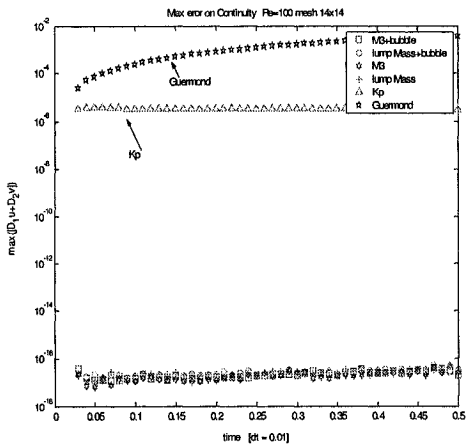

Figure 57
Re=100. Time evolution of continuity error.

For the forced flow, for Reynolds number unity, the Guermond's CPM shows remarkable accuracy in velocity (figure 49). This is consistent with the original authors finding with Stokes Flow [24]. As the Reynolds number is increased to 10 and 100, the other methods

attain higher accuracy (figures 50 and 51). All methods, except for the Guermonds CPM, showed similar errors for the velocity in this flow. For the pressure, the bubbles resulted in slightly decreased accuracy (figures 52, 53, 54) for the Reynolds numbers considered. The K_P method and lump mass method provided the highest accuracy for pressure. As for the error on continuity, Guermond's CPM performed poorly compared to the other methods which has much lower errors of similar values (figures 55, 56, 57).

6.2.2 On Spatial Distribution of Errors

The spatial error distribution is computed for t=0.5. The values obtained by equation (5.4) for the spatial error distribution for continuity and equation (5.5) for pressure is presented for Reynolds numbers 1, 10 and 100 below.

Re=1

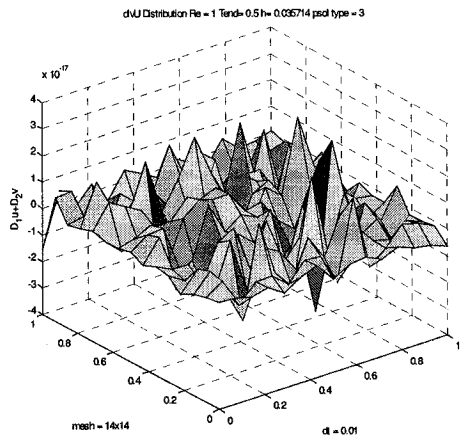

Figure 58
Re=1. M3+bubble continuity spatial error

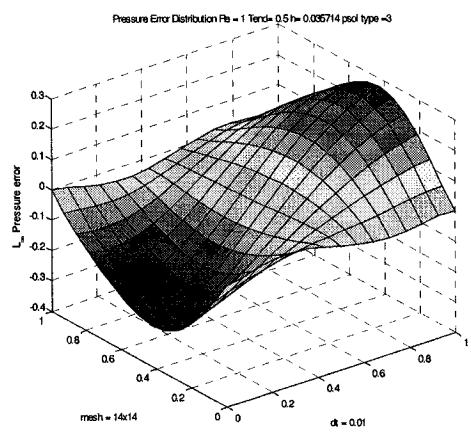

Figure 59
Re=1. M3+bubble pressure spatial error.

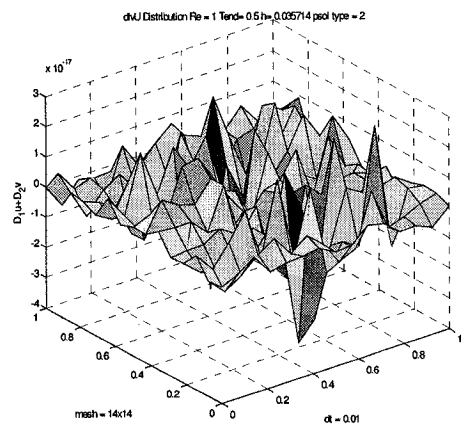

Figure 60
Re=1. lump Mass+bubble continuity spatial error.

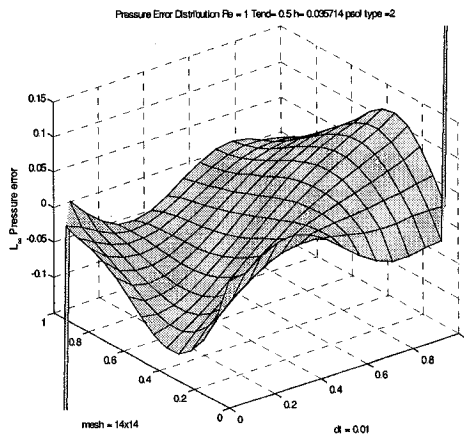

Figure 61
Re=1. lump Mass+bubble pressure spatial error.

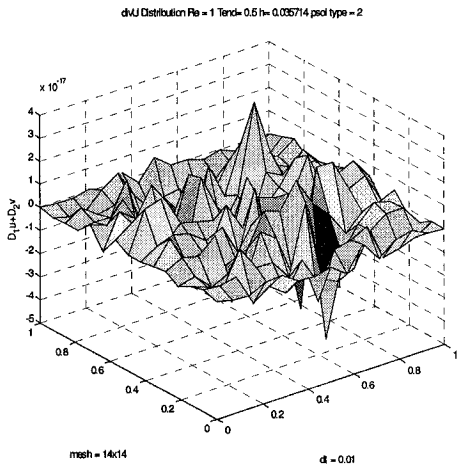

Figure 62
Re=1. lump Mass (no bubble) continuity error.

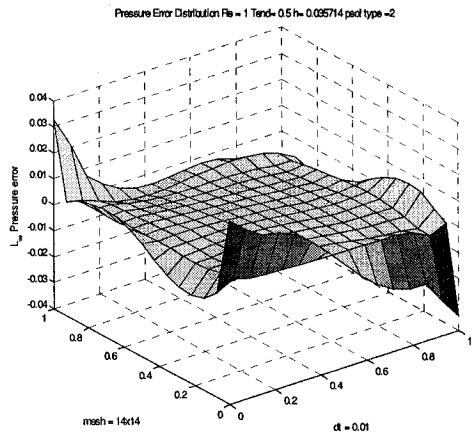

Figure 63
Re=1. lump Mass (no bubble) pressure error.

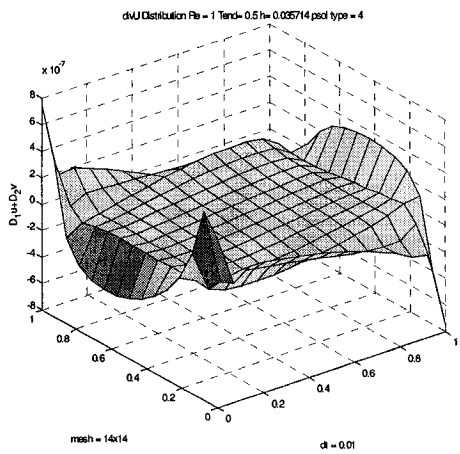

Figure 64
Re=1. K_P continuity spatial error.

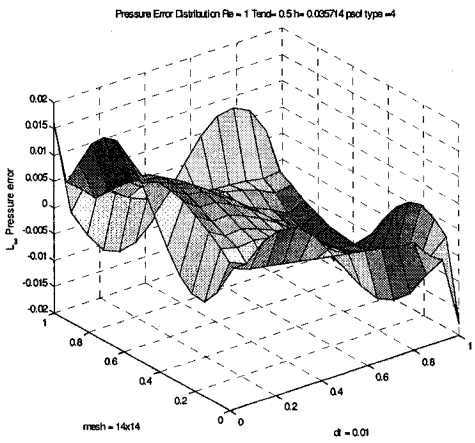

Figure 65
Re=1. K_P pressure spatial error.

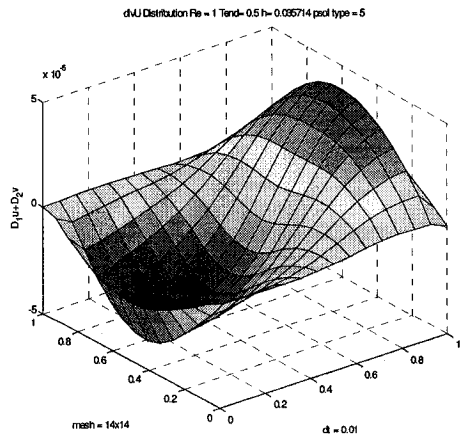

Figure 66
Re=1. Guermond continuity spatial error.

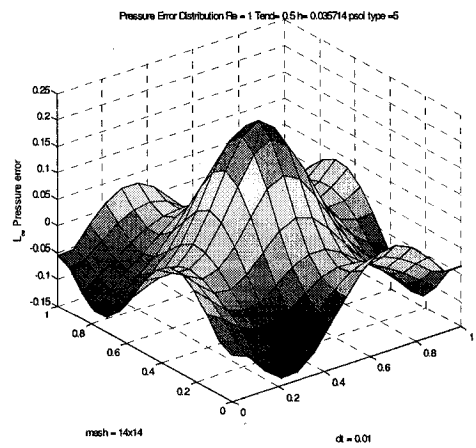

Figure 67
Re=1. Guermond pressure spatial error.

Re=10

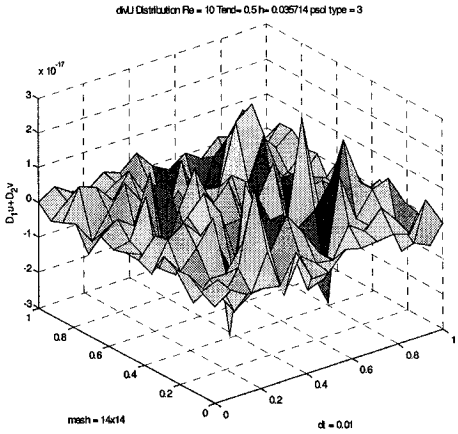

Figure 68
Re=10. M3+bubble continuity spatial error

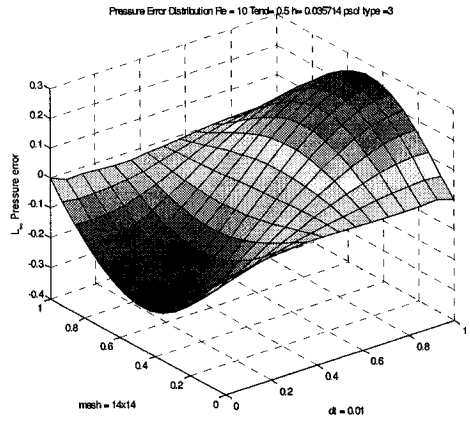

Figure 69
Re=10. M3+bubble pressure spatial error.

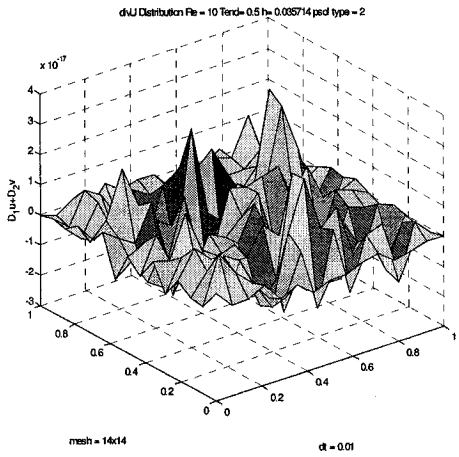

Figure 70
Re=10. lump Mass+bubble continuity error.

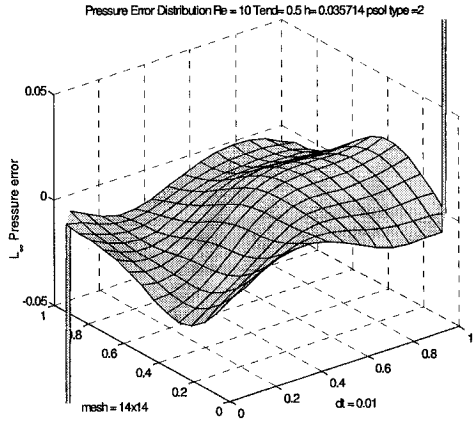

Figure 71
Re=10. lump Mass+bubble pressure error.

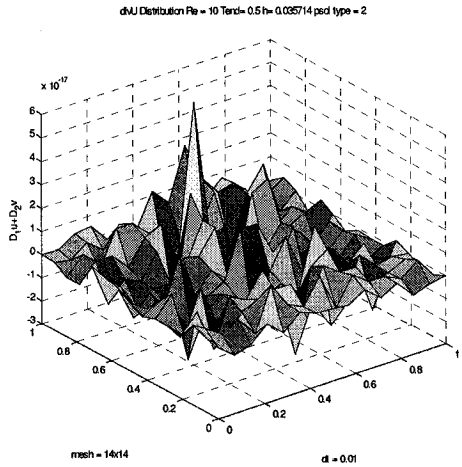

Figure 72
Re=10. lump Mass (no bubble) continuity error.

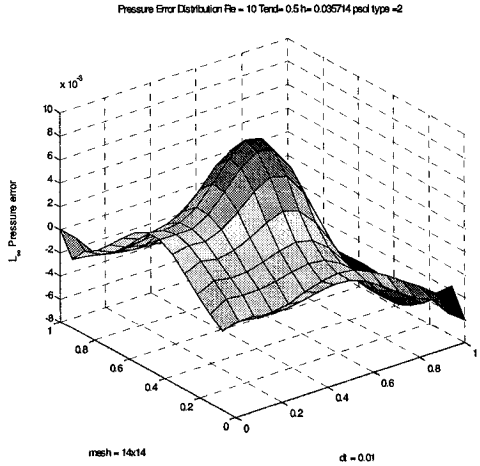

Figure 73
Re=10. lump Mass (no bubble) pressure error.

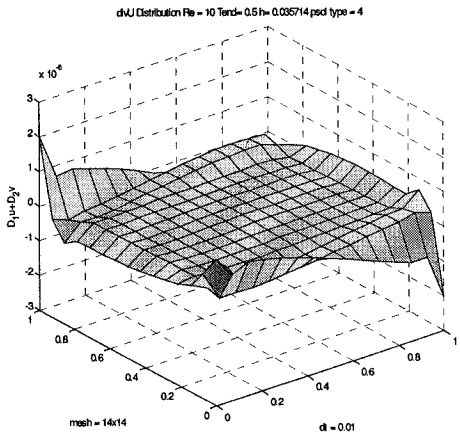

Figure 74
Re=10. K_P continuity spatial error.

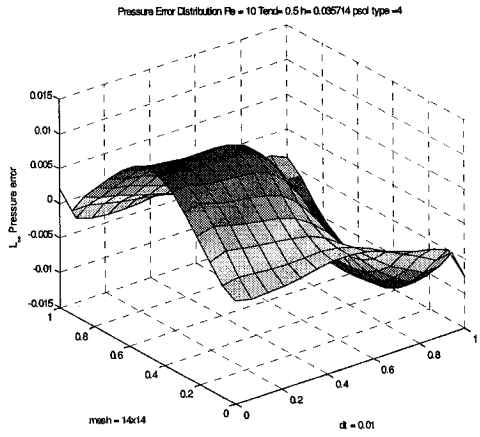

Figure 75
Re=10. K_P pressure spatial error.

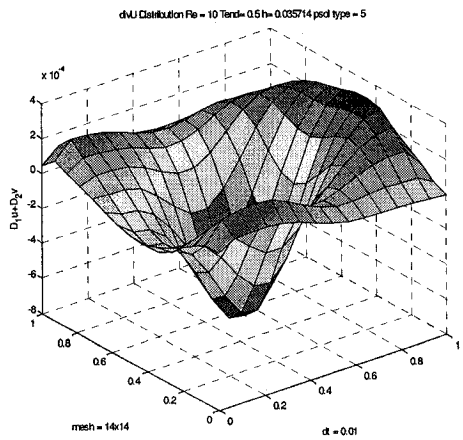

Figure 76
Re=10. Guermond continuity spatial error.

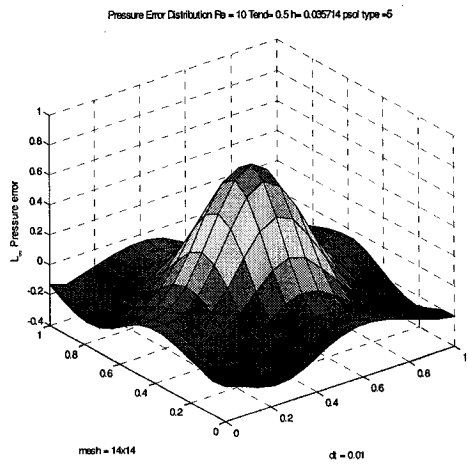

Figure 77
Re=10. Guermond pressure spatial error.

Re=100

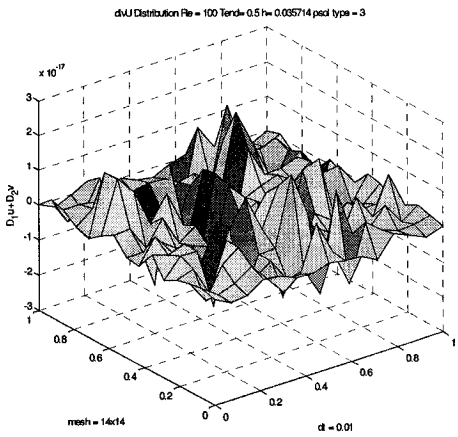

Figure 78
Re=100. M3+bubble continuity spatial error

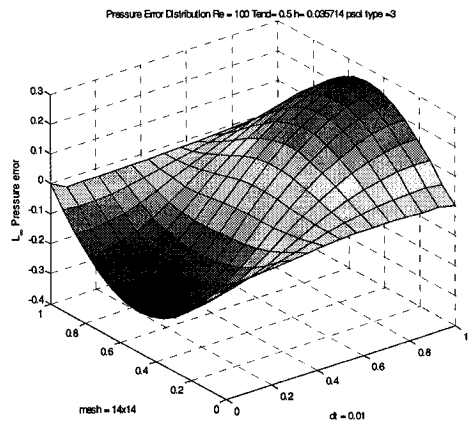

Figure 79
Re=100. M3+bubble pressure spatial error.

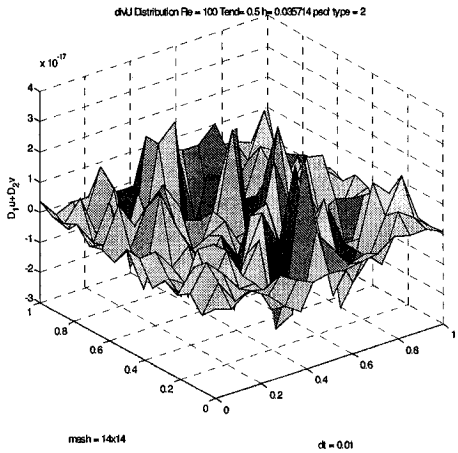

Figure 80
Re=100. lump Mass+bubble continuity error.

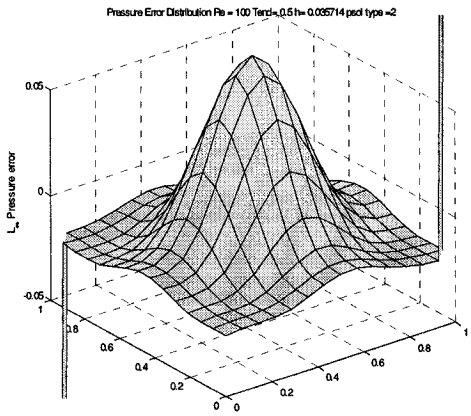

Figure 81
Re=100. lump Mass+bubble pressure error.

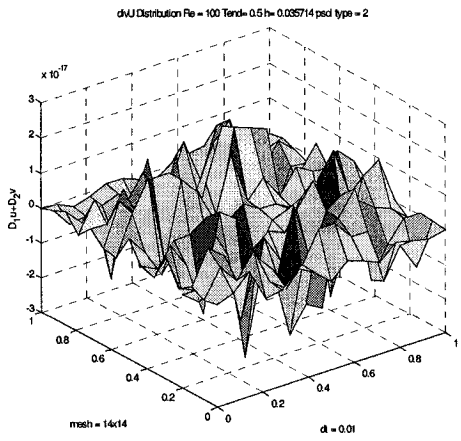

Figure 82
Re=100. lump Mass (no bubble) continuity error.

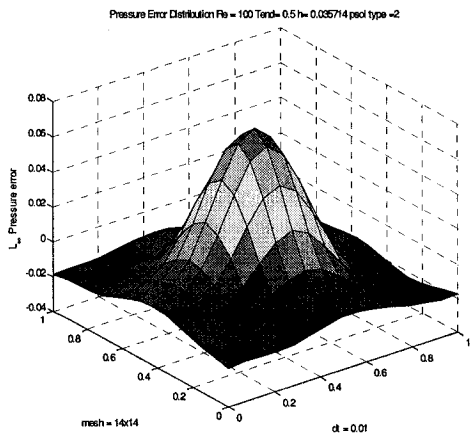

Figure 83
Re=100. lump Mass (no bubble) pressure error.

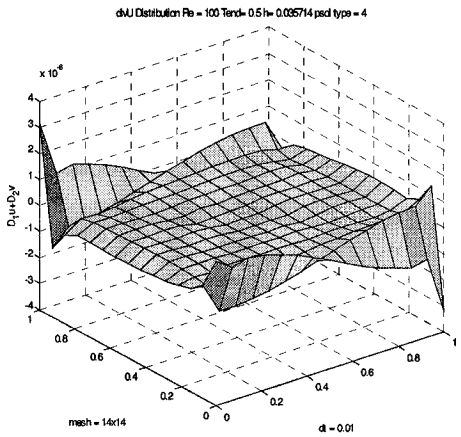

Figure 84
Re=100. K_P continuity spatial error.

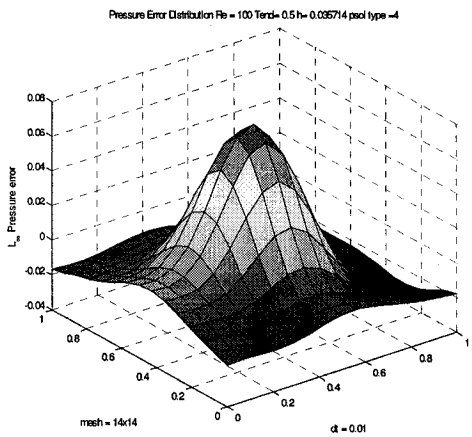

Figure 85
Re=100. K_P pressure spatial error.

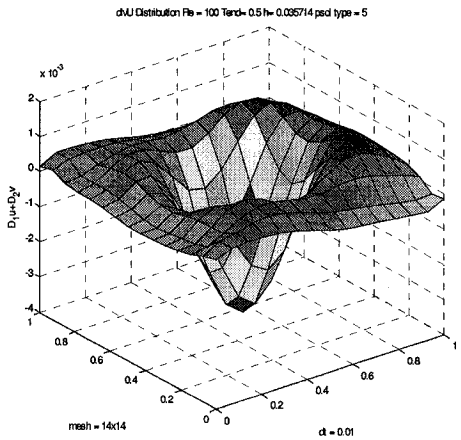

Figure 86
Re=100. Guermond continuity spatial error.

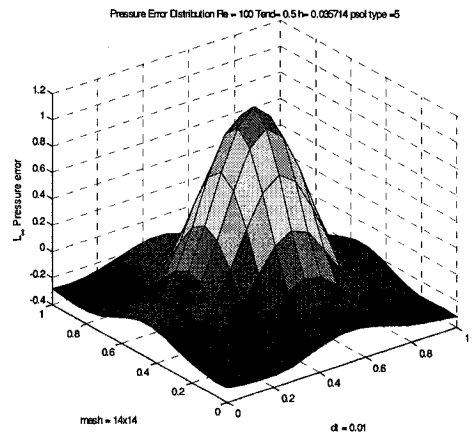

Figure 87
Re=100. Guermond pressure spatial error.

The error on continuity for the classical methods are found to be highly accurate (figures 58, 60, 62, 68, 70, 72, 78, 80, 82) confirming the previous study of maximum error revealed. There is a very small difference in the error of the pressure in M3 method as the Reynolds number is increased (figure 59, 69, 79).

At Reynolds numbers 1 and 10 the lump mass method (TH without bubble) shows a numerical boundary layer in pressure solution (figure 63, 73). The lump mass method with bubble-enriched elements however, does not show any increase in the error of pressure near the boundary (figure 61,71) although the overall L_2 error distributions of

them are higher than their no bubble counterparts. As the Reynolds number increased, the numerical boundary layer on lump mass method diminished and at Reynolds 100 altogether is disappeared (figure 81). The error due to the vortex flow however continues to grow as the Reynolds number is increased and is visible as a hump centred on the vortex.

The K_P method shows a numerical boundary layer in pressure as well as a corresponding error in the continuity field at Reynolds numbers 1 and 10 (figure 64, 65 and 74, 75). The numerical boundary layer disappears as the Reynolds number is increased to 100 yet the boundary error at continuity field remains. Unlike the numerical boundary layer near the walls, the error due to vortex remains in the pressure field and does not reflect in the continuity.

While Guermond's CPM shows no sign of the numerical boundary layer in the pressure field, the error due to the vortex flow grows rapidly with the Reynolds number figure 67, 77, 87). The error due to vortex flow is also reflected in the continuity field and grows with increasing Reynolds number (figures 76, 86). At Reynolds number of unity, the error in the continuity does not correspond to the vortex flow.

6.3 Lid Driven Cavity Flow

The Lid driven Cavity is defined by a domain $]0,1[^2$ with the Dirichlet boundary condition at the top edge as $u\,|_{\Gamma_{bottom}} = 1$. The remaining three edges are considered to be walls. An analytical solution to this flow is not available. The present study focuses on the imposition of the continuity on the flow solution. It is known that the robustness of the flow solver is depended upon how well the continuity equation is satisfied in the flow field.

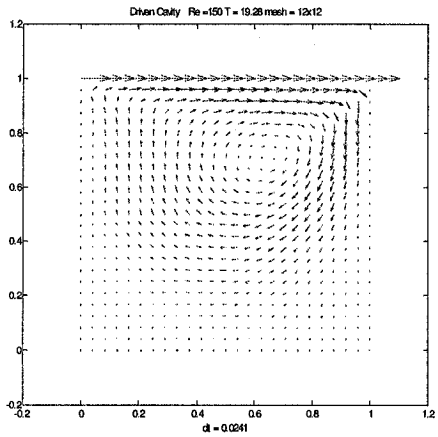

Figure 88
The velocity vector field of the Lid Driven Cavity flow at Reynolds number 150 Computed by M3 method.

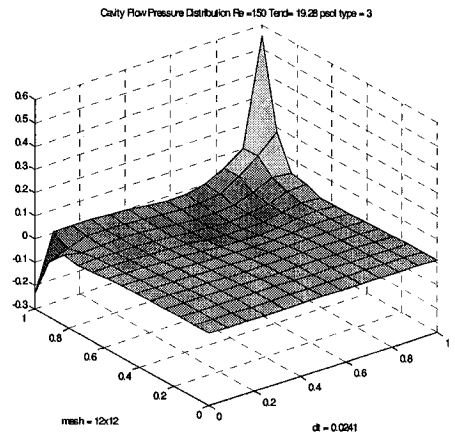

Figure 89
Pressure field of the Lid Driven Cavity Flow at Reynolds number 150 computed by M3 method.

The figure 88 and 89 shows an example vector field and a pressure field solution for the Lid Driven Cavity (we shall also refer to this flow as Cavity Flow for brevity). Note the singularities of the pressure solutions at the two edges that the driven lid makes with stationary walls.

6.3.1 Time evolution of Continuity error.

The time evolution of the error in continuity equation is conducted for the Lid Driven Cavity Flow. The maximum error is computed by equation (5.3). The time integration is performed with time step size well under the maximum allowed by the stability criteria of the integration scheme. The Reynolds numbers 1,10 and 500 are chosen to highlight the low Reynolds number effects and vorticity effects.

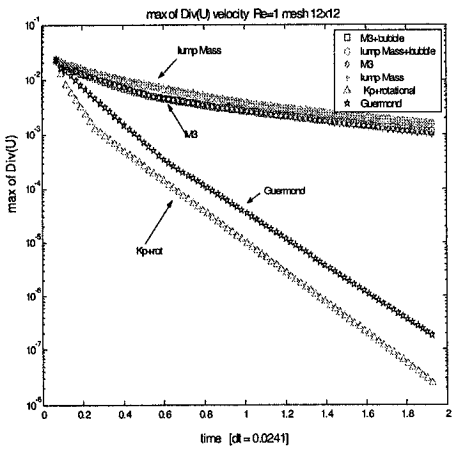

Figure 90
Re=1. Maximum error on continuity

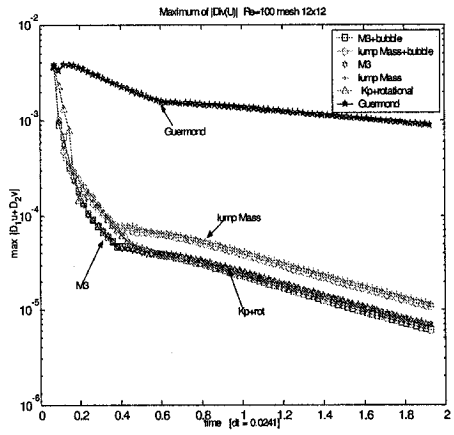

Figure 91
Re=100. Maximum error on continuity

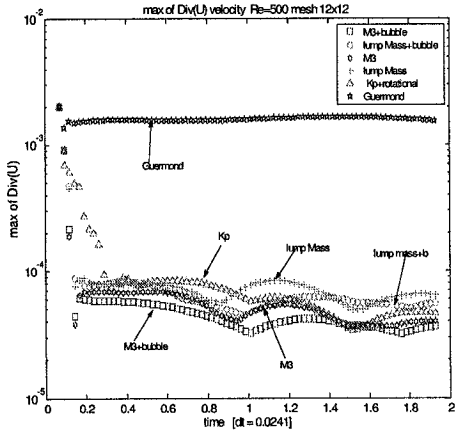

Figure 92
Re=500. Maximum error on continuity.

At Reynolds number of unity the K_P method and the Guermond's CPM obtains higher accuracy on the continuity constraint (figure 90) than the classical pressure methods. As the Reynolds number is increased the classical Pressure methods, M3 followed by lump mass, provides accurate continuity and the CPM provides the least accurate (figures 91, 92). The K_P method remains accurate through.

6.3.2 On Spatial Error Distribution

The spatial error analysis is performed for time t=9.9774, a sufficient time for the flow to approach a stationary state and also to allow sufficient iteration of the numerical scheme to enhance the cumulative spatial errors, namely the numerical boundary layer.

Re=1

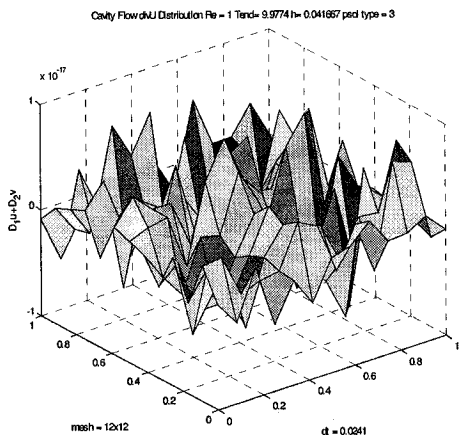

figure 93
Re-1. M3 Continuity spatial error

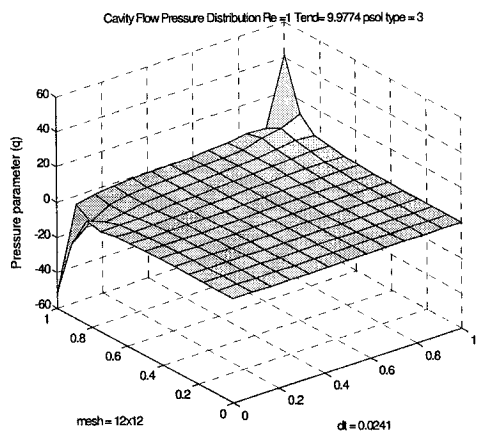

Figure 94
Re=1. M3 Pressure solution.

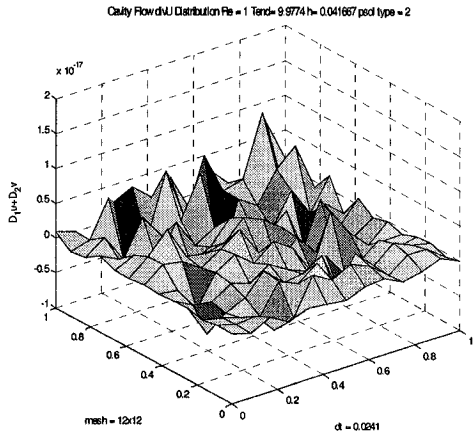

figure 95
Re-1. lump M (no bubble) Continuity spatial error

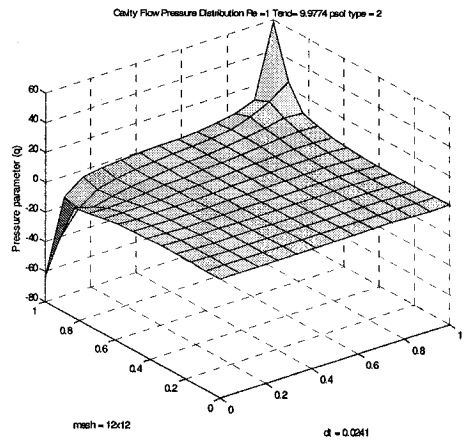

Figure 96
Re=1. lump M (no bubble) Pressure solution.

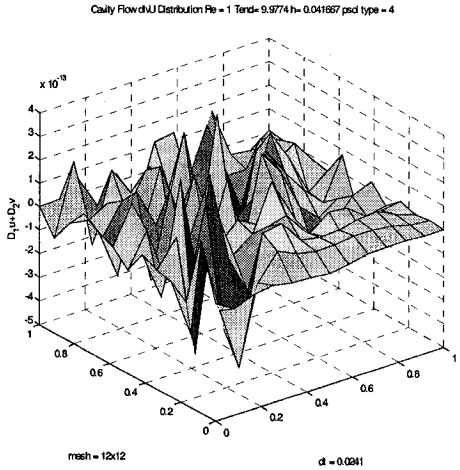

Figure 97
Re-1. K_P Continuity spatial error

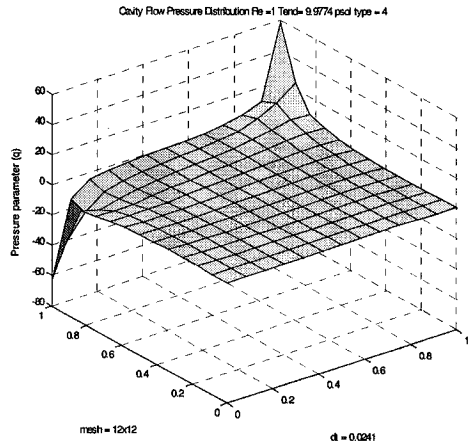

Figure 98
Re=1. K_P Pressure solution.

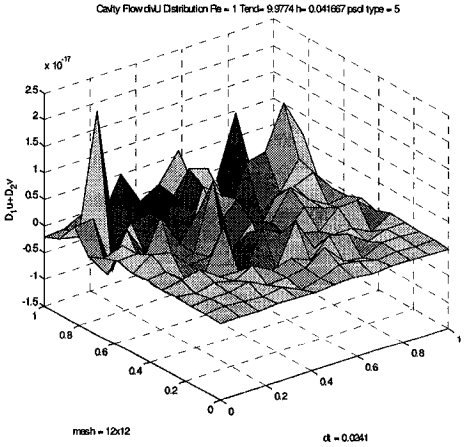

figure 99
Re-1. Guermond Continuity spatial error

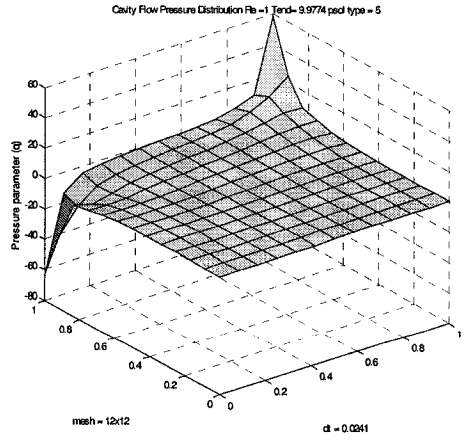

Figure 100
Re=1. Guermond Pressure solution.

Re=100

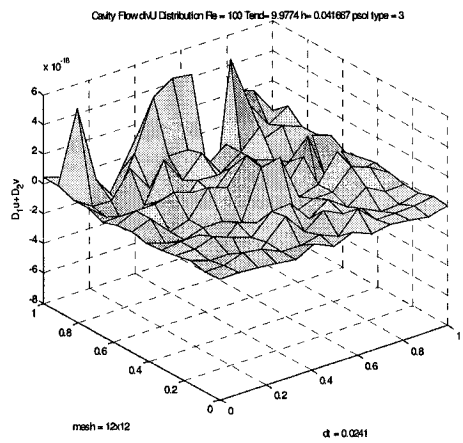

figure 101
Re-100. M3 Continuity spatial error

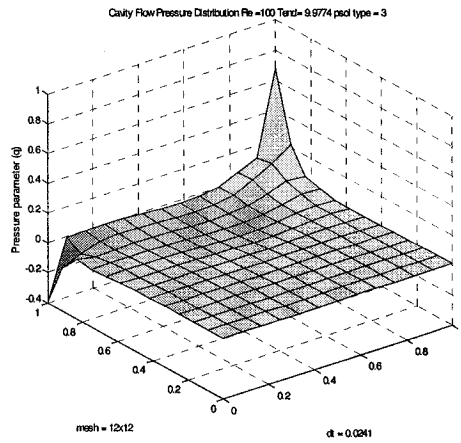

Figure 102
Re=100. M3 Pressure solution.

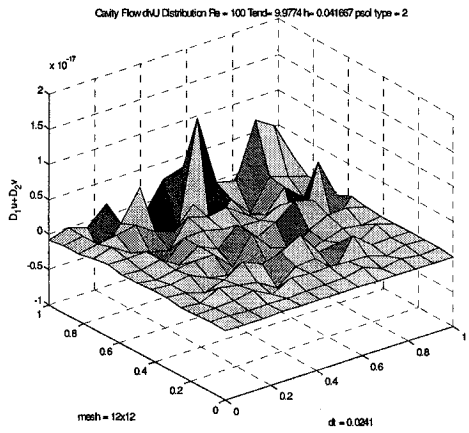

figure 103
Re-100. lump M (no bubble) Continuity error

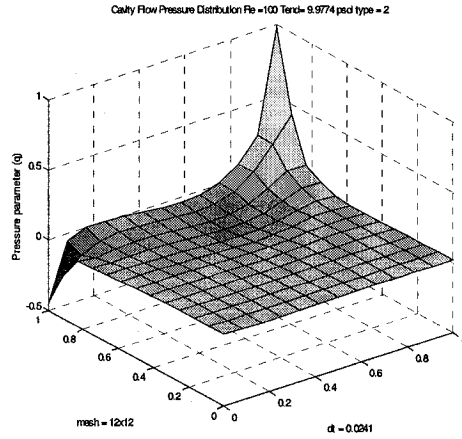

Figure 104
Re=100. lump M (no bubble) Pressure solution.

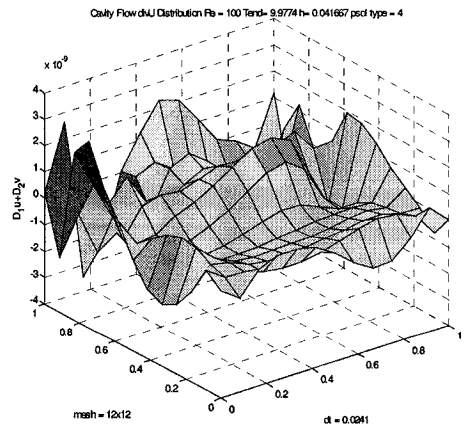

figure 105
Re-100. K_P Continuity spatial error

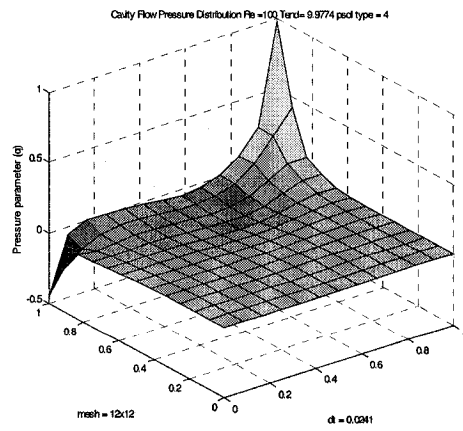

Figure 106
Re=100. K_P Pressure solution.

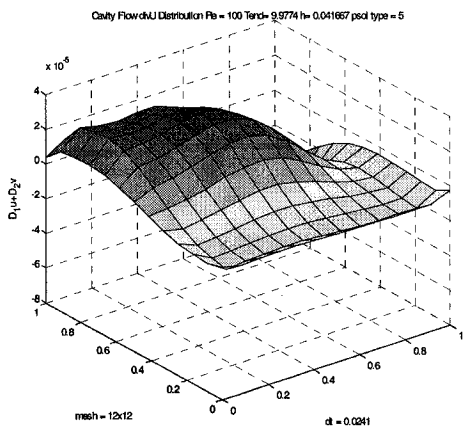

figure 107
Re-100. Guermond Continuity spatial error

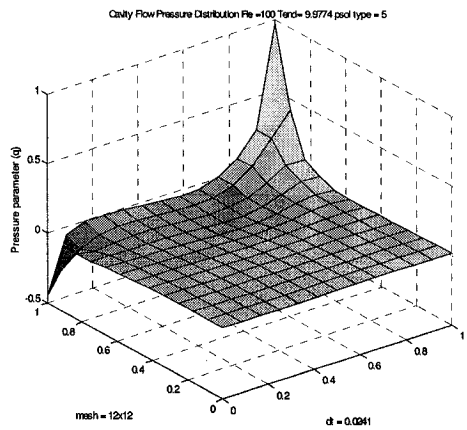

Figure 108
Re=100. lump Guermond Pressure solution.

Re=500

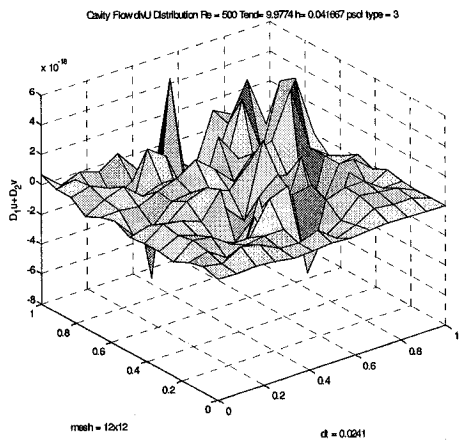

figure 109
Re-500. M3 Continuity spatial error

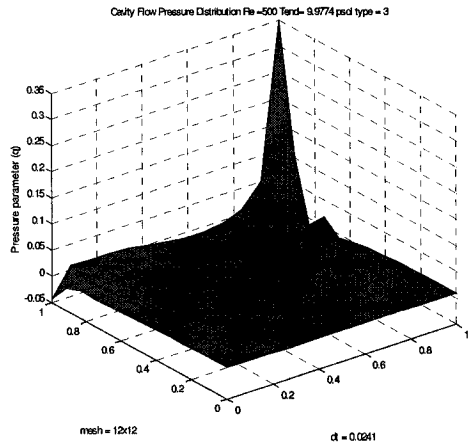

Figure 110
Re=500. M3 Pressure solution.

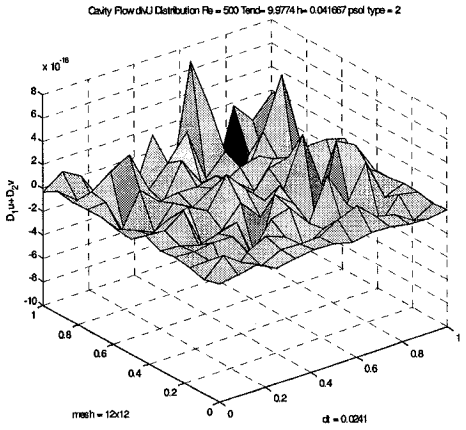

figure 111
Re-500. lump M (no bubble) Continuity error

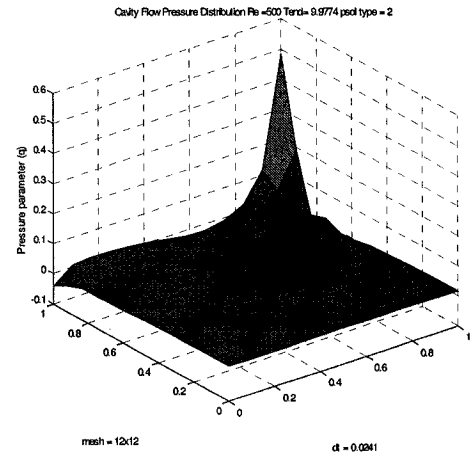

Figure 112
Re=500. lump M (no bubble) Pressure solution.

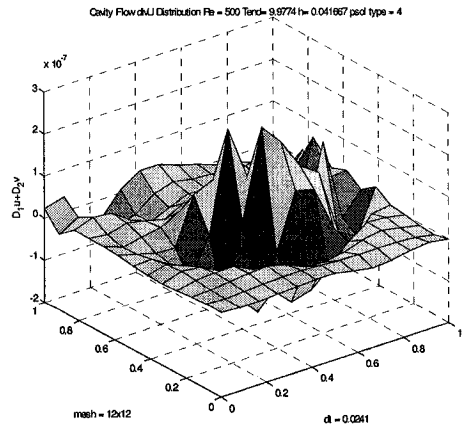

figure 113
Re-500. K_P Continuity spatial error

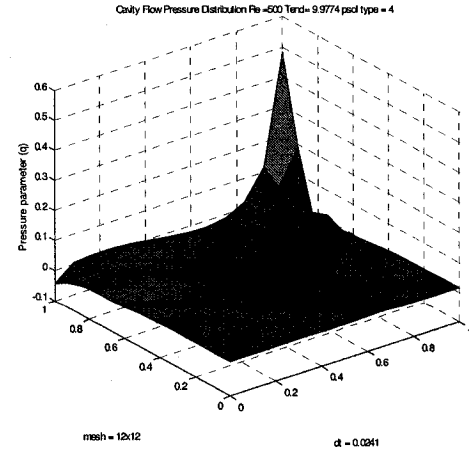

Figure 114
Re=500. K_P Pressure solution.

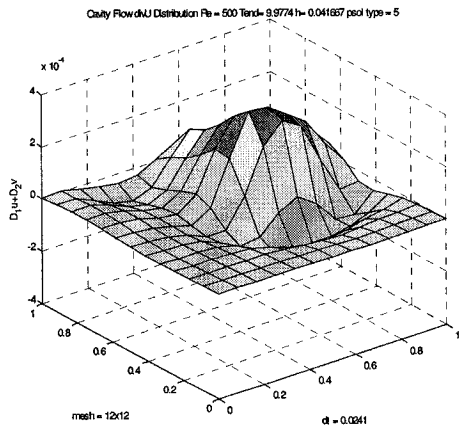

figure 115
Re-500. Guermond Continuity spatial error

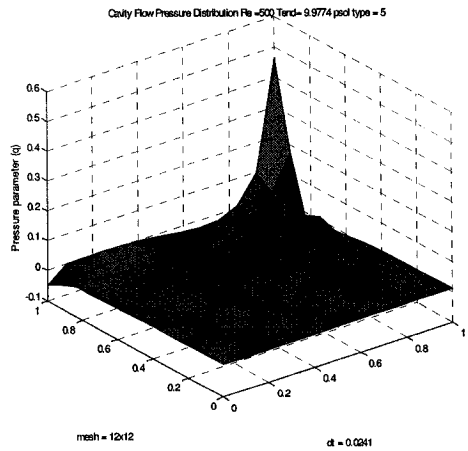

Figure 116
Re=500. Guermond Pressure solution.

As with the previous spatial error analysis of the continuity, the errors remain low for the classical pressure computation methods (figures 93, 94, 101, 103, 109, 111). At Reynolds number unity, the approximate pressure methods perform well in continuity as well (figures 97, 99). At Reynolds number 100, both K_P method and CPM shows what appears to be a numerical boundary layer on the continuity error field (figures 105, 107). Both methods also show errors in continuity in the middle corresponding the vortex. At Reynolds number 500, the errors in continuity of the K_P and CPM coincide with the vortex flow (figures 113, 115).

The pressure fields (figures 94, 96, 98, 100, 102, 104, 106, 108, 110, 112, 114, 116) show the pressure singularities in the lid-wall corners and the onset of a stronger vortex (the dip in the pressure) as the Reynolds number is increased. The magnitude of the pressure singularity decreased with increasing Reynolds Number. The magnitude of the M3 pressure singularity is lower than that of the other methods.

7 Analysis

7.1 Analysis and Conclusions

At high Reynolds numbers, methods that employ classical pressure computation techniques are found to be more accurate, or at least as accurate, in velocity and in their imposition of continuity than methods that employ approximate pressure computation techniques. The bubble nodes that are applied in computing the classical pressure update are found to be effective in improving the accuracy of the velocity and continuity. Both positive and negative effects of bubble nodes on the accuracy of pressure are observed for the Taylor-Green flow and in forced flow respectively. The bubble nodes eliminated the numerical boundary layer of the pressure in lump mass methods, though, while doing so, they increased the L_2 error of the pressure. The characteristic of the indirect pressure computed by M3 method however, does not differ much by bubble elements and does not contain a numerical boundary layer.

The approximate pressure methods are found to be less accurate in higher Reynolds number flow. Guermond's CPM shows promise in low Reynolds number flow and Stokes flow, but is not suitable for high Reynolds number flow when implemented with Taylor-Hood elements due to high error both in continuity and in pressure. CPM and K_P method with rotational pressure update are found to have correlated errors in pressure and in continuity in vortical flows. This attribute of the solvers could lead to difficulties when simulation of separated flows where the vorticity as well as the pressure gradient could reach to high values. The K_P method showed numerical boundary layer both in pressure and in velocity. The CPM does not show any numerical boundary layer for the forced flow, yet for the Driven Cavity Flow at Reynolds number 100, the continuity (figure 107) shows a distinct change of error in the boundary layer. This leaves the

possibility that for some flows CPM could have a numerical boundary layer. Further investigations of CPM with different flow are needed.

Corner errors, a very high error at corners due to the mesh connectivity there, are observed for the lump mass method with bubbles. By adjusting the bubble weight parameter, β , close to unity, the corner errors were greatly diminished.

The second order updating for the pressure, Type II and IV are found to be leading to instabilities and divergence.

Based on the above considerations, we shall conclude that, when implemented with Taylor-Hood elements, the Fractional Splitting Methods of Classical Pressure Computation type would yield more accurate solvers for high Reynolds number flows than Consistent Splitting type or FSM with Approximate Pressure Computations type would. The enrichment of the Taylor-Hood elements with pressure bubbles generally increases to accuracy of the solvers and remove the pressure numerical boundary layer. Due to generally higher accuracy and some observed advantages in robustness the classical pressure update methods of FSM, lump mass method and Mixed Mass Matrix (M3) method remains strong candidates for a highly accurate, robust and computationally efficient solver for modern application such as Large Eddy Simulations. Guermond's CPM remains a good method for low Reynolds number flow or Stokes flow.

7.2 Future Work

The present work motivates further investigation of enriching the Taylor-Hood elements with pressure bubbles. The implication that bubble nodes can remove pressure boundary layer and possibilities such as β/P-adaptation could lead to fruitful future investigations.

The success of classical pressure updating methods, such as the proposed M3 method, would require further work into computing the correct pressure as well as the general problem of correct implementation of the pressure boundary conditions.

The correct implementation of boundary conditions, including the inlet/exit boundary conditions, has received attention recently [22] and work on this direction would yield a code that is suitable for modern applications such as Large Eddy Simulations and Direct Numerical Simulations of turbulent flow.

Bibliography

[1] A. Aris, *Vectors, Tensors and the Basic Equations of Fluid Mechanics.* Dover Publications, New York (1989)

[2] G. K. Batchelor, *An Introduction to Fluid Dynamics.* Cambridge University Press, New York (2000)

[3] J.B. Bell, P. Colella, and H.M. Glaz, *A second order projection method for incompressible Navier-Stokes equations.* J. Comput. Phys. **85**, 257 (1989)

[4] M. Benzi, G. H. Golub, J. Liessen, *Numerical solution of Saddle Point Problems.* Acta. Numerica pp1-137 (2005)

[5] D. Braess, *Finite Elements, Theory, fast solvers and applications in solid mechanics.* Cambridge University Press, Cambridge (2001)

[6] S. C. Brenner, L. R. Scott, *The Mathematical Theory of Finite Elements.* Springer-Verlag, New York (2002)

[7] D. L. Brown, *Accuracy of Projection Methods for the Incompressible Navier-Stokes Equations.* Workshop on Numerical Simulation of Incompressible Flows, Half Moon Bay, CA June (2001)

[8] D. L. Brown, R. Cortez and L. Minon, *Accurate Projection Method for the Incompressible Navier-Stokes Equations.* Journal of Computational Physics **168**, 464-499 (2001)

[9] G. A. Cardenas Casas, *Large Eddy Simulation using Tetrahedral Finite Elements.* MASc Thesis, University of Toronto (2003)

[10] A.J. Chorin,*Numerical solutions of the Navier-Stokes equation.* Math. Comp.,22:745-762, (1968)

[11] A. J. Chorin, *Vorticity and Turbulence.* Springer-Verlag, New York (1994)

[12] M. O. Deville, P. F. Fisher, E. H. Mund,. *High Order Methods for Incompressible Fluid Flow.* Cambridge University Press, Cambrdge, UK (2002)

[13] J. Donea, A. Huerta, *Finite Element Method for Flow Problems.* John Wiley and sons, West Sussex, England (2003)

[14] W. E and J.G. Liu, *Gauge Method for viscous incompressible flows.* Commun. Math. Sci., 1(2):317-332 (2003).

[15] R. Lohner, *Applied CFD Techniques, An Introduction based on Finite Element Method.* John Wiley and sons, West Sussex, England (2001)

[16] H. C. Elman, G. H. Golub, *Inexact and Preconditioned Uzawa Algorithms For Saddle Point Problems.* SIAM J. Numer. Anal 31(6) 1545-1661 (1984)

[17] Franca, Farhat, Comp. Metd. Appl. Mech. Eng (1995)

[18] U. Ghia, K. N. Ghia, C. T. Shin, *High Re Solutions for incompressible flow using the Navier Stokes equations and multigrid method.* J. Comput. Phys. 40 ,(387) (1982)

[19] P.M. Gresho, R.L. Sani, *On Pressure Boundary conditions for incompressible Navier-Stokes equations,*Int. J. Numer. Methods Fluids, 7 (1987) 1111-1145

[20] M. Griebel, T. Dornseifer, T. Neunhoeffer, *Numerical Simulations in Fluid Dynamics.* SIAM press, Philadelphia (1998)

[21] J. L. Guermond, A., Marra, L. Quartapelle, *Subgrid stabilized projection method for 2D unsteady flows at high Reynolds numbers.* Pre-print (2005)

[22] J. L. Guermond, P. Minev, J. Shen, *An Overview of Projection Methods for Incompressible Flows.* To appear in Comp. Meth. Appl. Mech. Enfng. (2006)

[23] J.L. Guermond, P. Minev, J. Shen, *Error Analysis of pressure-correction schemes for the Navier-Stokes equations with open boundary conditions.* SIAM J. Numer. Anal. 43, 239-258 (2005)

[24] J. L. Guermond, J. Shen. *A new class of truly consistent splitting schemes for incompressible flows.* J. Comput. Phys., 192:262-276 (2003)

[25] M. Gunzburger, *Finite Element Methods for Viscous Incompressible Flow: A Guide to Theory, Practice and Algorithms.* Accademic Press, Boston (1989).

[26] D. J. Higham, N. J. Higham, *Matlab Guide.* SIAM press, Philadelphia (2000)

[27] T. J. R. Hughs, *The Finite Element Method.* Dover Publications, Mineola, NY (2000)

[28]. J. Kim, P. Monin, *Application of fractional-step method to incompressible Navie,-Stokes equations,* J. Comp. Phys. **59** (1985), 308-323

[29] M. B. Monagan, K. O. Geddes, G. Labahn, V. Vorkoetter, *Maple V Programming Guide.* Waterloo Maple-Springer (1996)

[30] .S.A. Orszag, M. Israeli, and M.O. Deville, *Boundary conditions for incompressible flows.* J. Sci. Comput. **1**. 75 (1986)

[31]. M. Picasso, J. Rappaz, *Stability of Time-Splitting Schemes for the Stokes Problem with Stabilized Finite Elelments.*pre-print (2000)

[32]. J. N. Reddy, D. K. Gartling, *The Finite Element Method in Heat Transfer and Fluid Dynamics*. CRC Press, New York (2001)

[33]. G. Strang, *Linear Algebra and its Aplications,* Academic Press, New York (1976)

[34] .G. Strang, G. J. Fix, *An Analysis of the Finite Element Method.* Wellesley-Cambridge Press, Wellesley, MA (1988)

[35] J.C. Strikwerda, Y.S. Lee, *The accuracy of the fractional step method.* SIAM. J. Numr. Anlal, 37(1) 37-47 (1999)

[36] Z. Sultana, *A Preconditioned Itarative Parallel Solver for the Incompressible Navier-Stokes Equations.* MASc Thesis, University of Toronto (2003)

[37] R. Temam., *Navier Stokes Equatons: Theory and Numerical Analysis.* North-Holland, Amsterdam (1984)

[38] J. W. Thomas, *Numercal Partial Differential Equations.* Springer-Verlag, New York (1995)

[39] L. N. Trefethen, D. Bau, *Numerical Linear Algebra.* Siam Press, Philadelphia (1997)

[40] H. A. Van Der Vorst, *Itarative Krylov Methods for Large Linear Systems.* Cambridge University Press, Cambridge (2003)

[41] J. Van Kan, *A second order accurate pressure-correction scheme for viscous incompressible flows,* SIAM J. Sci. compt. **7**, 870 (1986)

Appendix A

On Pressure update types

The second order pressure update is investigated here. The Classical methods were updated with Type II and K_P and CPM are updated by type IV. The M3 is left alone.

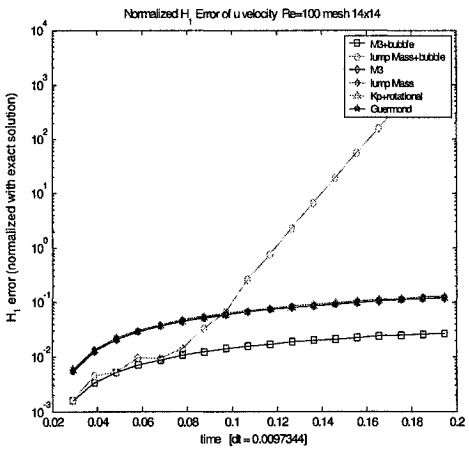

Figure A1
Re=100, velocity error with
2nd order pressure update

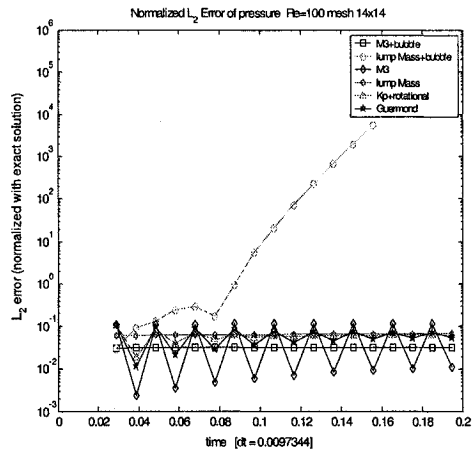

Figure A2
Re=100, pressure error with
2nd order pressure update

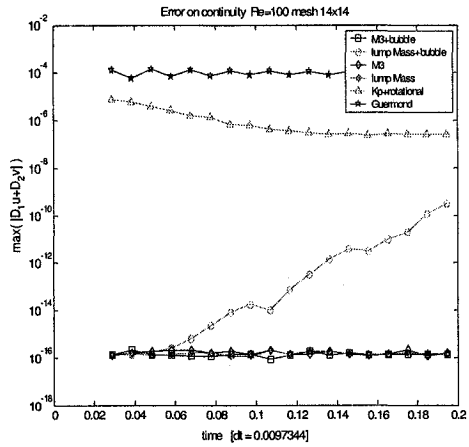

Figure A3
Re=100, continuity error with
2nd order pressure update.

The above are compared to figures 09, 12, 15 where first order pressure update is used. The second order pressure update is observed to be leading to instability.

Appendix B

Some Validations and Miscellaneous flow

Lid Driven Cavity

The Mixed Mass Method, introduced in current work is compared for the solutions of Driven Cavity Problem obtained by Ghia et. al. [18]. The above authors used a 256x256 multigrid method to generate the solution field. The curves below are obtained by 30 x 30 TH elements (no bubble) using M3 method.

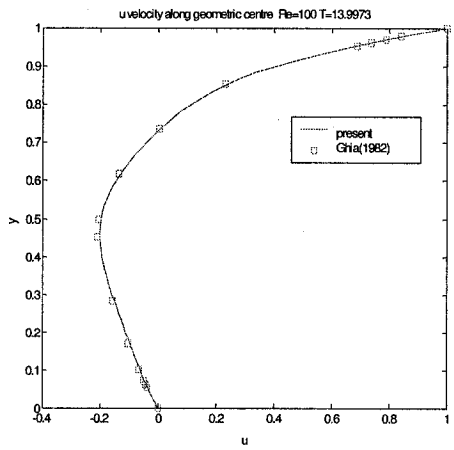

Figure 1B
U velocity along the centreline Y

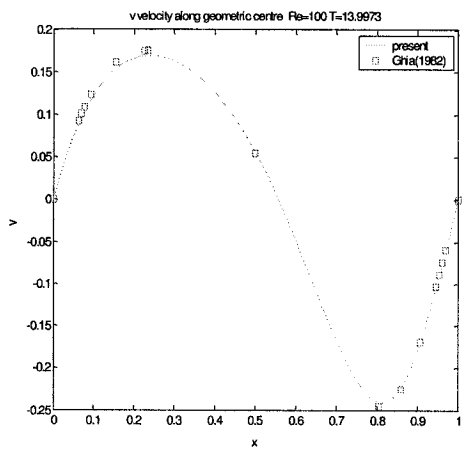

Figure 2B
V velocity along the centreline X

A small difference between the published work of Ghia and present simulation is observed at the peak velocities. This is due to coarseness of the mesh used in present study.

Cylinder in a Cross Flow

The robustness of the schemes is tested on the Cylinder in a Cross Flow simulation.

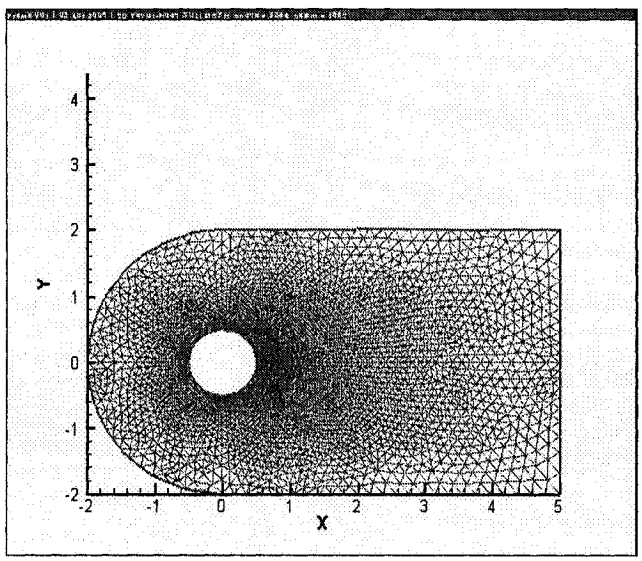

Figure 3B
The mesh used for the cylinder in a cross flow simulations.

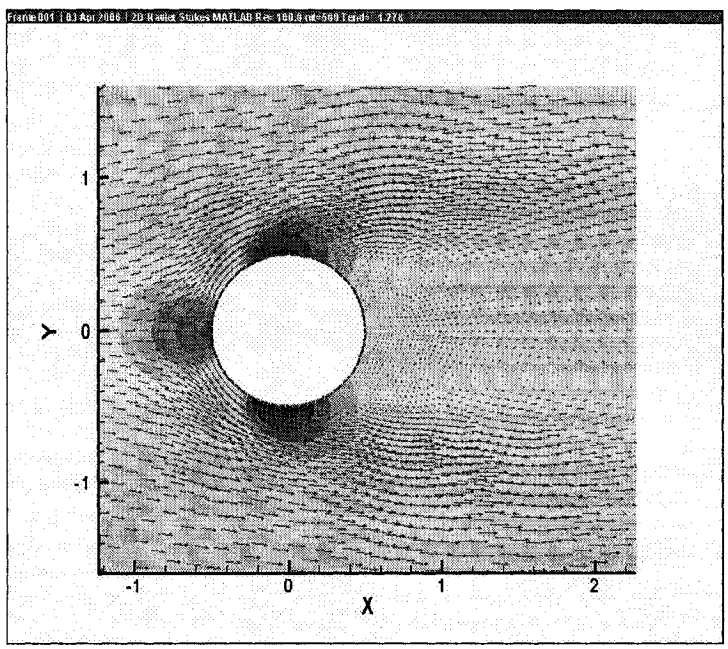

Figure 4B
The solution obtained for Re=100 using M3 method.

Mixed Mass Method (M3) in 3D

M3 is implemented in three dimensional computer program in C language.

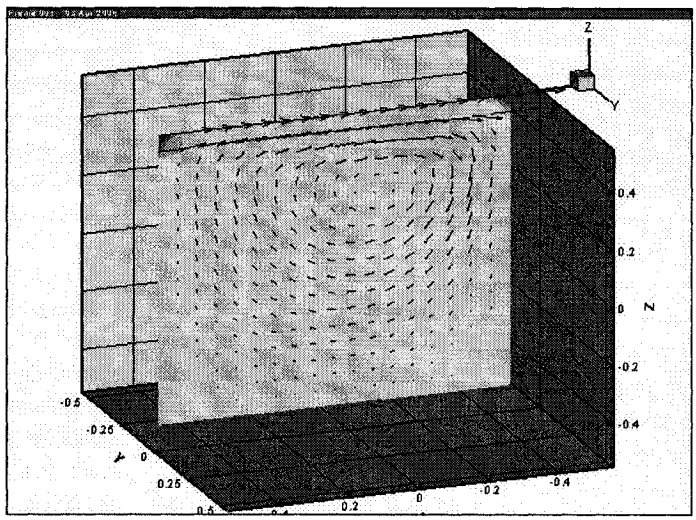

Figure 5B
Slice of flow field in 3D version of M3 code.

Appendix C

On Spatial Convergence

The forced flow with Reynolds number equal to 10 is re solved with a finer mesh of 20 x 20. This is in contrast to the studies on the main body of this work where mesh used is 14x14.

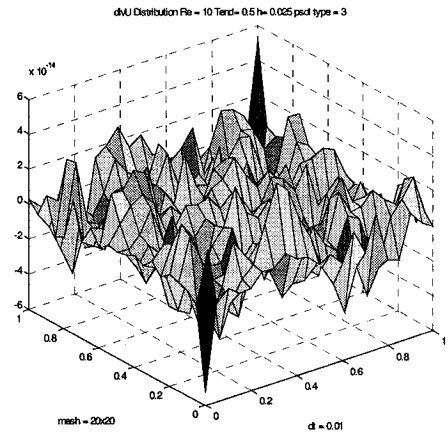

Figure 1C
Re=10, M3+bubble continuity spatial error

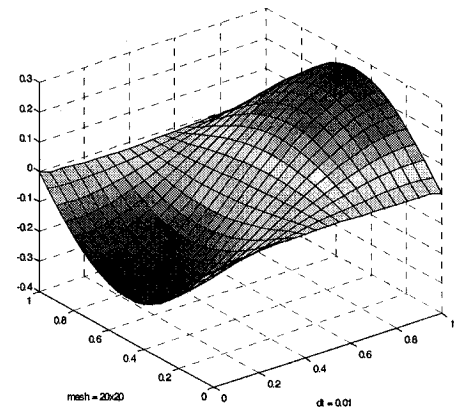

Figure 2C
Re=10, M3+bubble pressure error.

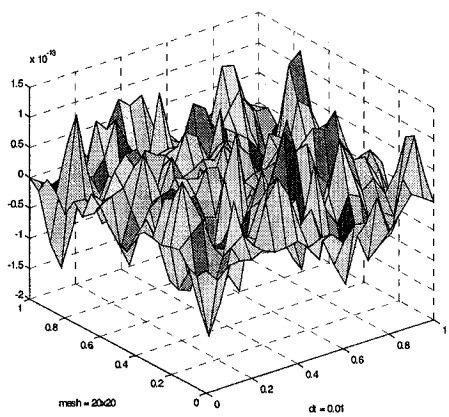

Figure 3C
Re=10, lump mass+ bubble continuity error

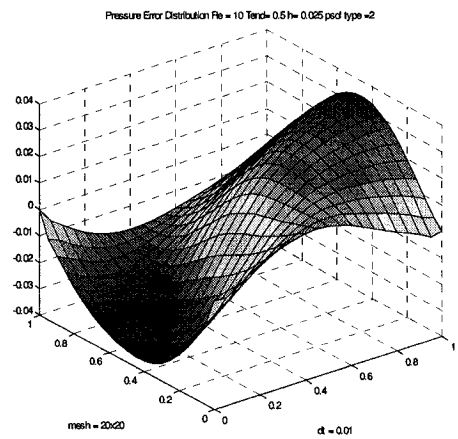

Figure 4C
Re=10, lump mass+bubble pressure error

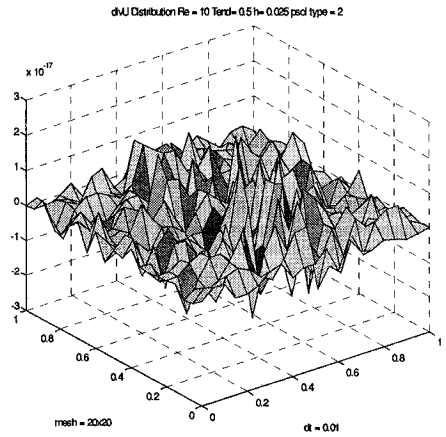

Figure 5C
Re=10, lump mass continuity spatial error

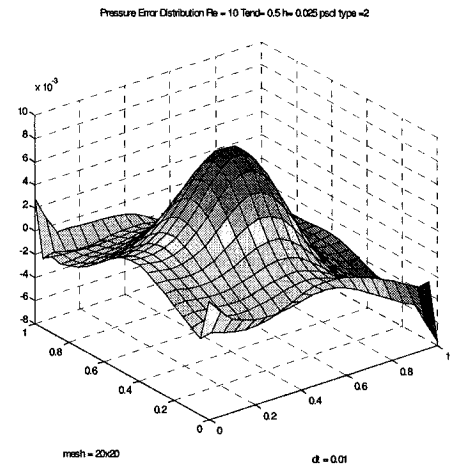

Fgure 6C
Re=10, lump mass pressure spatial error.

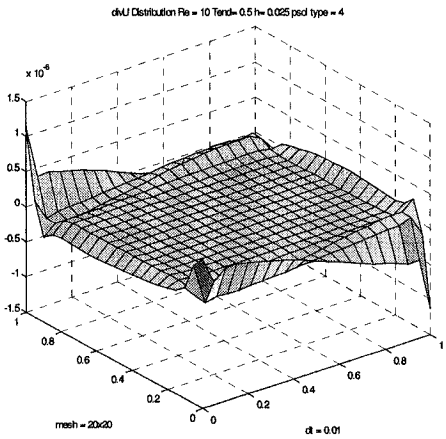

Figure 7C
Re=10, K_P continuity spatial error

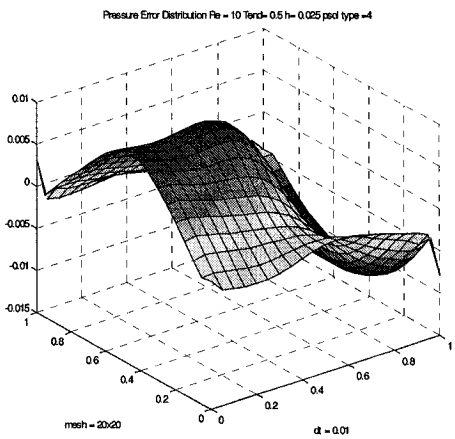

Figure 8C
Re=10, K_P, pressure spatial error

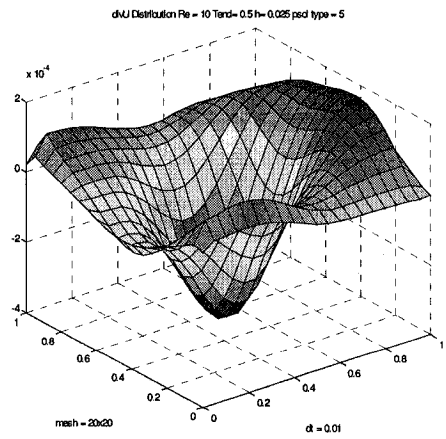

Figure 9C
Re=10. Guermond continuity spatial error.

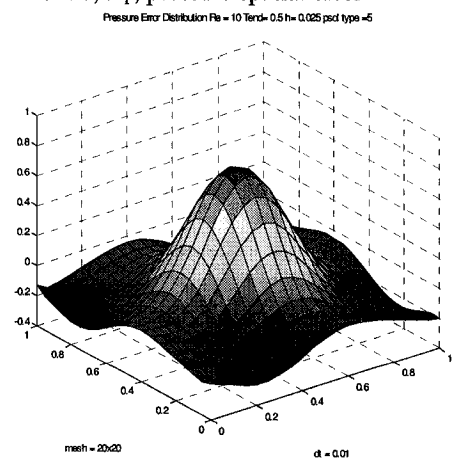

Figure 10C
Re=10. Guermond pressure spatial error.

The above plots, figures 1C to 10C (run with 20x20 mesh), in comparison with the plots of the Reynolds number 10 runs in section 6.2.2 that is run with a mesh of 14x14 (figure number 68 through 77) indicates that the characteristics of errors observed are not that of the mesh property but of the solver.